The interaction of parallel and inclined planar rarefied sonic plumes—From free molecular to continuum regime

Vesper, J. Elin; Broeders, Theo J.M.; Batenburg, Joëlle; van Odyck, Daniel E.A.; Kleijn, Chris R.

DOI
10.1063/5.0056730

Publication date
2021

Document Version
Final published version

Published in
Physics of Fluids

Citation (APA)
Vesper, J. E., Broeders, T. J. M., Batenburg, J., van Odyck, D. E. A., & Kleijn, C. R. (2021). The interaction of parallel and inclined planar rarefied sonic plumes—From free molecular to continuum regime. *Physics of Fluids*, *33*(8), Article 086103. https://doi.org/10.1063/5.0056730

Physics of Fluids

The interaction of parallel and inclined planar rarefied sonic plumes—From free molecular to continuum regime

Cite as: Phys. Fluids **33**, 086103 (2021); https://doi.org/10.1063/5.0056730
Submitted: 13 May 2021 . Accepted: 09 July 2021 . Published Online: 04 August 2021

J. Elin Vesper, Theo J. M. Broeders, Joëlle Batenburg, Daniel E. A. van Odyck, and Chris R. Kleijn

The interaction of parallel and inclined planar rarefied sonic plumes—From free molecular to continuum regime

Cite as: Phys. Fluids **33**, 086103 (2021); doi: 10.1063/5.0056730
Submitted: 13 May 2021 · Accepted: 9 July 2021 ·

J. Elin Vesper,[1,2,a)] Theo J. M. Broeders,[1] Joëlle Batenburg,[1] Daniel E. A. van Odyck,[3] and Chris R. Kleijn[1,2]

AFFILIATIONS

[1]Department of Chemical Engineering, Delft University of Technology, van der Maasweg 9, 2629 HZ Delft, The Netherlands
[2]J.M. Burgerscentrum for Fluid Dynamics, Mekelweg 2, 2628 CD Delft, The Netherlands
[3]Tata Steel, R&D, P.O. Box 10000, 1970 CA IJmuiden, The Netherlands

[a)]Author to whom correspondence should be addressed: j.e.vesper@tudelft.nl

ABSTRACT

The interaction between rarefied vapor plumes can cause shocks and consequently distinct peaks in mass flux which produce undesirable non-uniformities. To evaluate the impact of shock formation, we study pairs of interacting planar plumes, varying the degree of rarefaction and general geometric parameters, namely, the nozzle-separation-distance and the mutual plume inclination. To consider the extremes of rarefaction, we give the analytic solution for free molecular flow and simulate the inviscid continuum solution using an approximate Riemann solver. In the transitional flow regime, direct simulation Monte Carlo is applied. To detect the shock location, we make use of the Method of Characteristics. We conclude that, although the rarefied flow regime physically lies in between the free molecular and the inviscid continuum flow regimes, the peak value of mass flux in the transitional flow regime exceeds both the one of free molecular flows and the one of inviscid continuum flows (the latter by ≈10%). Rarefied flow exhibits a broader, but weaker secondary expansion after the shock than continuum flow. For planar jet interaction, the occurrence of the shock is rather insensitive to nozzle separation distance. Despite the intuitive expectation that inclining the plumes away from each other would lead to shock reduction and thus give a more uniform mass flux, the opposite is the case: Inclining the plumes toward each other leads to a stronger shock, but also to a stronger expansion, thus producing a more uniform mass flux with less stray mass fluxes.

NOMENCLATURE

$a = \sqrt{\gamma R T}$	Speed of sound $\mathrm{m\,s^{-1}}$
$\boldsymbol{c} = (c_x, c_z)$	Fluctuational velocity $\mathrm{m\,s^{-1}}$
c_p	Specific heat $\mathrm{J\,K^{-1}\,kg^{-1}}$
D	Length of inlet m
E_{kin}	Macroscopic kinetic energy J
E_{tot}	Total energy J
e	Specific internal energy $\mathrm{J\,kg^{-1}}$
$\boldsymbol{F}$	Deformation gradient tensor $\mathrm{m^{-1}}$
f	Phase density $\mathrm{s^6/m^3}$
f_0	Maxwellian distribution $\mathrm{s^6/m^3}$
h	Specific enthalpy $\mathrm{J\,kg^{-1}}$
Kn	Knudsen number
k_B	Boltzmann constant $1.380\,649 \times 10^{-23}\,\mathrm{J\,K^{-1}}$
L	Nozzle separation distance m
M	Mach number
m	Particle mass kg
n	Number density $\mathrm{m^{-3}}$
p	Pressure Pa
$\boldsymbol{R}$	Rotation matrix
R	Specific gas constant $\mathrm{J\,kg^{-1}\,K^{-1}}$
$\boldsymbol{r} = (x, z)$	Point vector m
t	Time s
$\boldsymbol{u}$	Macroscopic velocity $\mathrm{m\,s^{-1}}$
w	Regression weight

Greek

α	Inclination angle °
Γ^+, Γ^-	Characteristics
γ	Heat capacity ratio

Θ	Angular component of polar coordinates °
λ	Mean free path m
μ	Mach angle °
ν	Prandtl–Meyer angle °
ξ	Particle velocity $\mathrm{ms^{-1}}$
ρ	Density $\mathrm{kg\,m^{-3}}$
τ	Mean collision time s
ϕ	Flow angle °
Ω	Integration domain

Subscripts

in	Quantity at the inlet
L	Lower jet
S	Stagnation quantity
U	Upper jet

Superscripts

*	In critical section, i.e., $\mathrm{M} = 1$

I. INTRODUCTION

In recent years, clusters of rarefied vapor plumes (also sometimes called jets) have played an increasing role in both space and vacuum technology: The reaction control systems of shuttle orbiters operate with multiple exhaust plumes. Micro-satellites use plume clusters as well, and the number of launches has increased rapidly over the last decade.[1] Linear aerospike engines consisting of two planar plumes, which expand along the two sides of a spike and merge at the spike's end, are a promising rocket and micro-satellite thruster technology. This design of two interacting plumes can compensate for the decreasing atmospheric pressure and consequently suppress the increase in expansion at higher altitudes, allowing for single-stage-to-orbit space vehicles.[2] Recently, clusters of sonic zinc vapor plumes have been introduced as a novel technology to achieve a continuous physical vapor deposition (PVD) apparatus for galvanizing steel.[3,4] For all these technologies, the fluxes from the plumes are of importance. Shuttle orbiters operate next to space stations; the momentum flux and the heat flux from the exhaust plumes may cause damage when impinging on any sensitive structures, such as solar panels or optically sensitive components.[5,6] In coating technology, highly uniform coating is desirable, which requires a uniform mass flux from the deposition plumes.

However, interacting plumes may cause a shock, which results in mass flow and temperature peaks around the interaction plane. The subsequent high-pressure region between the shocks leads to another expansion, called a "secondary jet." From the secondary jet, a backflow may emerge which, for aerospikes and thrusters, gives a pressure and heat load on the surface of the propelled space vehicle itself. In addition, recirculation in the interaction plane introduces viscous losses and may reduce the efficiency of thrusters.[7]

Single plumes are thoroughly studied due to their ubiquitous use as thrusters in aerospace.[5,8,9] Backflows appear for plume thrusters, especially for small Mach numbers, since then the expansion angle at the nozzle exit lip is obtuse and the flow is redirected toward the space vehicle. The resulting forces can disturb the space vehicle orientation and the heat flux and contamination may damage the vehicle's surface. Several researchers studied the backflow and suggested designs to minimize it.[10–13] Plume interaction may increase the backflow and the subsequent contamination of the space vehicle. Tools based on CFD (Computational Fluid Dynamics), Direct Simulation Monte Carlo (DSMC), and approximations have been developed to predict the contamination, heat flux, and disturbance forces due to plume impingement.[14–17] Recently, extraterrestrial plumes were simulated and compared to their appearance in space.[18–20]

Plume interaction has so far been much less studied. Since measurements in moderate or high vacuum conditions are difficult, only a few experiments of plume interaction are reported in the literature, mainly considering space thrusters. Depending on the process conditions, researchers found density peaks around the interaction plane.[21,22,69] Some observed a small backflow.[22] To determine the occurrence of a shock and its strength under rarefied conditions, Koppenwallner[23] (as cited by Dagum and Zhu[24]) introduced the penetration Knudsen number Kn_p, as the ratio of the mean free path in the interaction plane and the path length between the interaction plane and the axis of the other plume. A few groups confirmed that the penetration Knudsen number is indeed a determining parameter for the occurrence of a shock under particular circumstances.[25,26] However, Dagum and Zhu[24,27] studied parallel plume interaction at different nozzle separation distances using the direct simulation Monte Carlo (DSMC) method and found that the penetration Knudsen number could not predict the shock impact on the flow field. For three interacting planar aluminum vapor plumes (aligned in one row), Venkattraman and Alexeenko[28] found that the deposition profile can be described by a superposition of the deposition of three single plumes at high Knudsen numbers, whereas at smaller Knudsen numbers the deviation due to the interaction peak is immense. Baby and Rajesh[29] studied jet interaction for two three-dimensional jets at a moderate pressure ratio ($r_p \approx 2500$–9500) and a background pressure of 5 Pa, which yields barrel shocks which inhibited the interaction between the jets. Although some simulations and experiments for specific designs and flow conditions were reported in the literature,[30–32] a comprehensive evaluation of the sensitivity of the mass flux distribution to geometry and process conditions is missing. This knowledge is crucial for applications in propulsion systems, but also for coating technology, where non-uniformities caused by jet interaction deteriorate the product.

To execute such a comprehensive evaluation, we study the onset, location, and strength of the shock caused by two interacting planar sonic plumes of zinc vapor, as depicted in Fig. 1, depending on the geometry and process conditions, to make statements about the uniformity of mass flow at a most general level. The rarefaction ranges from the high Knudsen number free molecular to the low Knudsen number inviscid continuum flow limit.

In Sec. II, we introduce the solution methods, such as analytic equations for free molecular effusion flow, an approximate Riemann solver for inviscid continuum flow and direct simulation Monte Carlo (DSMC) for the transitional flow regime. The Methods section also describes the shock detection method, the far-field approximation, and a discussion on the Penetration Knudsen number. The exact geometry, boundary conditions, and thermophysical properties are discussed in Sec. III. In Sec. IV, the flow fields for free molecular and continuum flow are compared to those for rarefied flow. Afterward, the shock location method is introduced and the effect of rarefaction on the shock location discussed. The shock location method is

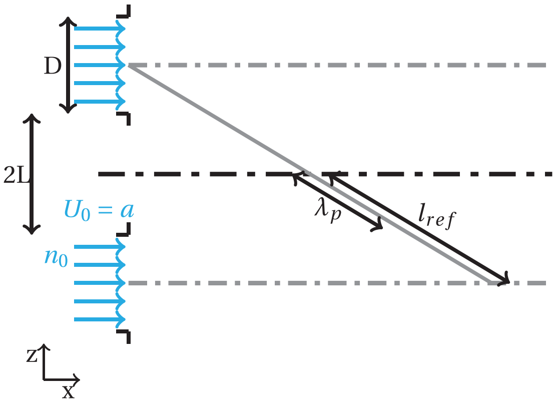

FIG. 1. General flow setup: Plumes emerge from two inlets of length D at a nozzle separation distance $2L$. The domain extends infinitely in the third direction causing a planar problem. The penetration Knudsen number is defined as $Kn_p = \lambda_p/l_{ref}$.

validated by analyzing the shock structure in relation to the detected shock location. To evaluate the influence of the shock on the mass flux distribution, mass flux profiles are compared for different degrees of rarefaction. Afterward, shock location and line profiles are discussed for the other varied parameters, i.e., nozzle-separation distance and plume inclination. Finally, we compare the deposition uniformity for coating applications depending on these parameters.

II. METHODS

The phase density $f(\mathbf{r}, \mathbf{c}, t)$ describes the probability of finding a molecule at location $\mathbf{r}$ with velocity $\mathbf{c}$ at time t. The evolution of the phase density f is governed by the Boltzmann equation which, in the absence of body forces, reads as

$$\frac{\partial f(\boldsymbol{r}, \boldsymbol{\xi}, t)}{\partial t} + \boldsymbol{\xi} \cdot \nabla_{\boldsymbol{r}} f(\boldsymbol{r}, \boldsymbol{\xi}, t) = \left(\frac{\partial f(\boldsymbol{r}, \boldsymbol{\xi}, t)}{\partial t}\right)_{coll}, \tag{1}$$

where the left-hand side describes the convective transport and the right-hand side the collisions between particles. In Sec. II A, only the left-hand side of Eq. (1) is considered, giving us the collisionless or free molecular flow. In Sec. II B, the local equilibrium case is described, which means that f in Eq. (1) is replaced by the Maxwellian distribution f_0. Integrating the moments of this simplified equation over the velocity space leads to the Euler equations shown in Sec. II B. For the steady-state Euler equations in the supersonic regime, the Method of Characteristics (MOC) describes the flow field, which we used for the shock detection presented and which can be seen as the basis for approximate Riemann solvers. Section II C describes how to solve Eq. (1) for rarefied gases in the transition regime—where there are too many collisions to neglect the collision operator on the right-hand side, but too few to assume Maxwellian or Chapman–Enskog velocity distributions (which would yield the Euler and Navier–Stokes–Fourier equations, respectively). Section II D sets out the far-field solution for the planar case (as the solutions given in the literature apply to a three-dimensional jet), which is used for the penetration Knudsen number described in Sec. II E.

A. Analytic collisionless solution

The collisionless flow solution provides the extreme case of rarefaction as well as an insight into the non-equilibrium resulting from velocity sorting. The first analytical solution for free molecular flow from one slot was outlined by Knudsen[33] in 1909. He based his cosine law for the so-called Knudsen cell on an equilibrium assumption and zero mean velocity at the slot outlet, which is not true for our case as the vacuum accelerates the flow and thus directs it along the jet axis, producing a higher density around the jet axis and a lower density far away from it. It was only in the 2000s that Cai and Boyd proposed an exact collisionless solution, which includes both the spatial extension of the inlet and a non-zero inlet velocity.[34] We adapted their solution for a single straight jet to the two inclined jets by altering the integration domain and superposition, and the details are given in Appendix A.

B. Continuum flow

Continuum flows are most commonly described by the Navier–Stokes–Fourier equations, which correspond to the first-order Chapman–Enskog approximation of the Boltzmann equation and include shear stress and heat flux. Yet for free expansions of supersonic plumes into vacuum, convective forces greatly surpass viscous forces (i.e., the Reynolds number tends to infinity, which yields a flow field similar to the inviscid limit) and no walls are present to form shear boundary layers. Since the velocity gradient is aligned with the flow direction in many parts of the flow field, the impact of shear stress is expected to be low. With the Prandtl number of gases $\approx 2/3$ being close to unity, also thermal conduction is expected to play a minor role in the energy equation compared to convection. Therefore, viscous forces and conductive heat fluxes can be neglected in a first approximation (i.e., using a Maxwellian distribution instead of the first-order Chapman–Enskog expansion). The Navier–Stokes–Fourier equations then reduce to the Euler equations

$$\frac{\partial \rho}{\partial t} + \nabla \cdot (\rho\, \mathbf{u}) = 0\,, \tag{2}$$

$$\frac{\partial}{\partial t}(\rho\, \mathbf{u}) + \nabla \cdot (\rho\, \mathbf{u} \otimes \mathbf{u}) = -\nabla \bar{p}\,, \tag{3}$$

$$\frac{\partial}{\partial t}(\rho\, e) + \nabla \cdot [(\rho\, e + p)\mathbf{u}] = 0\,, \tag{4}$$

where the specific energy is $e = e_{int} + 0.5\mathbf{u}^2$ and the enthalpy is $h = e_{int} + p/\rho$ is used to calculate the temperature field. We close the equations by assuming a calorically perfect gas, i.e., $h = c_p T$ and $p/\rho = RT$.

1. Method of characteristics

For purely supersonic flow, the Euler equations exhibit a hyperbolic behavior in space, which implies that information propagates in a wave-like manner. In a steady-state case as ours, the downstream solution depends only on the upstream solution and can be deduced from it by using the Method of Characteristics (MOC). A proper derivation can be found in the book by Vos and Farokhi;[35] here, we briefly sketch the underlying physics. In our case, the uniform inflow is homentropic and homenergetic, which according to Crocco's theorem entails that the flow field is irrotational.[36] This condition breaks inside the shock where the entropy increases and, consequently, the flow becomes rotational. The following qualitative visualization is confined to the planar, irrotational MOC and, strictly speaking, is therefore not applicable after the shock. The local velocity vector is sufficiently described by the local speed and flow direction expressed by the Mach number M and the flow angle φ. The local information propagates along the flow direction with the flow speed $a \cdot M$ and orthogonal to it with the speed of sound a. Therefore, the domain of influence of each point is the Mach cone which expands around the streamline with the Mach angle,

$$\mu = \sin^{-1}\left(\frac{1}{M}\right). \tag{5}$$

The left-running Γ^+ and right-running Γ^- characteristics span the Mach cone around the streamline as symmetry axis. Figure 2 sketches a streamline with the corresponding characteristics for one point. The Prandtl–Meyer function $\nu(M)$ indicates the angle, through which a sonic flow turns when it accelerates to a certain Mach number M greater than 1. A fluid element, which accelerates isentropically from Mach number M_1 to Mach number M_2, turns its direction by an angle $\nu(M_2) - \nu(M_1)$ (a compression proceeds inversely).

Along the characteristics Γ^+ and Γ^-, the following linear combinations of the flow angle and the Prandtl–Meyer-function are constant:

$$\nu - \varphi = \text{const. along}\,\Gamma^+ : \frac{dz}{dx} = \tan(\varphi + \mu), \tag{6}$$

$$\nu + \varphi = \text{const. along}\,\Gamma^- : \frac{dz}{dx} = \tan(\varphi - \mu), \tag{7}$$

where φ depends on the location as well as ν and μ, which are the functions of the local Mach number.

Figure 3 shows the MOC solution for a sonic plume and a qualitative sketch of how the plume interaction modifies the solution (the non-isentropic process across the shock complicates a completely analytic solution and the presence of the subsonic region suppresses it entirely (see Zucrow on backward-facing step[37]). At the corners of the inlet, expansion fans arise, depicted by the characteristics emerging from the corners and spreading into the domain. The flow turns outward toward the vacuum and accelerates. It changes when crossing one of the depicted expansion fan lines, whereas within each of the polygons depicted in Fig. 3, the Mach number and flow direction as well as density, pressure, and temperature are approximated to be homogeneous (finer spatial discretization, i.e., more expansion fan lines emerging from the inlet corners, tends toward the correct solution). The flow direction is along the half angle between the Γ^+ and Γ^- characteristics and exemplary depicted by vectors in blue. In the core of the plume, the interaction of the characteristics deflects them, but their expansion character remains, i.e., the characteristics are diverging downstream. Due to the presence of an identical second plume next to the first one in our problem, the case is symmetric. At the symmetry axis, the velocity normal to it has to be zero, and on the left side, immediately after the inlets, the velocity aligned with the symmetry axis is small, which results in a subsonic region. The flow from the expansion fan impinges on the concave part of the subsonic region causing compression waves which in turn induce a shock. Both the compression waves and the shock run along Γ^+ characteristics. The shock propagates through the velocity field. While around the subsonic region, the incoming flow is nearly orthogonal to the shock producing a (nearly) normal shock, further downstream the incoming flow has a significant tangential component to the shock resulting in an oblique shock. When crossing the shock, the Γ^- characteristics slightly bend toward the symmetry axis, where they are reflected and hit the shock a second time from its downstream side. Since the characteristics remain expansion waves both after crossing the shock and after the reflection at the symmetry, they bend the shock away from the symmetry axis.[38]

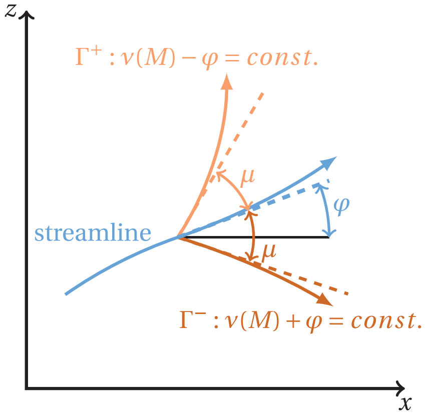

FIG. 2. Schematic of characteristics.

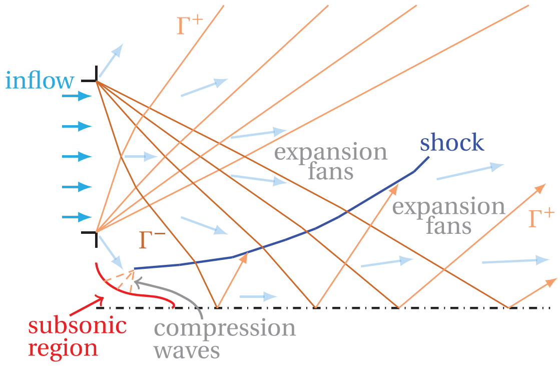

FIG. 3. Qualitative sketch of plume interaction explained by Method of Characteristics. Expansion fans emerge from the inlet corners. The interaction between the flow and the subsonic region causes compression waves which induce a shock. The characteristics from the expansion bend when crossing the shock and get reflected at the symmetry.

Except for the subsonic region, the entire flow field is described by the Mach number M and the flow angle φ. The inviscid Euler solution is thus independent of the temperature and density (which can be deduced along the streamlines using isentropic relations), so that—except for a change in the shape of the subsonic region depending on density—the inviscid continuum flow field depends only on the nozzle separation distance and inclination.

2. Detection of shocks and characteristics

Commonly, shocks are identified as regions with a high density of pressure isolines or with a pressure gradient magnitude above a specified value.[72] However, the rapid expansions in the problem under consideration give rise to high-pressure gradients before the shock and consequently strongly varying shock strength along the shock (we use the common shock strength definition as the pre- to post-shock pressure ratio). This complicates the shock detection based on the pressure field. A further obstacle is finite shock thickness, as a shock extends over several mean free paths [$\mathcal{O}(10)$] and the mean free path in rarefied flow is long.[39] Kanamori and Suzuki[40,41] proposed to detect the shocks as a singularity in the characteristics field given by the local unit vectors in the direction $\mathrm{d}z/\mathrm{d}x$ from Eqs. (6) and (7). As shown in Sec. II B 1, the compression waves, which are $\boldsymbol{\Gamma}^+$ characteristics inclined toward each other, merge forming the shock. Anticipating the characteristics presented in Fig. 8, we see that also other $\boldsymbol{\Gamma}^+$ characteristics inciding on the shock, merge with it, producing a local sink in the $\boldsymbol{\Gamma}^+$-field. Thus, a strong divergence in the $\boldsymbol{\Gamma}^+$ field indicates a shock. The broader shock in the transitional flow regime makes the algorithm by Kanamori and Suzuki more difficult to apply. This is why we base our implementation only loosely on their approach.

First, the deformation gradient tensor of the $\boldsymbol{\Gamma}^+$ field is calculated in all supersonic regions. Then, the region with negative divergence of the $\boldsymbol{\Gamma}^+$ field, i.e., the sink, is extracted. From this subset, we extract the regions where the deformation gradient tensor of $\boldsymbol{\Gamma}^+$ projected into the flow direction is negative. This second clipping is necessary, to exclude regions in which the divergence is negative due a gradient orthogonal to the streamlines (which occurs abundantly around the point where the sonic line cuts the symmetry) rather than along the streamlines. From this shock region, a shock line is derived by quartic regression weighted with the magnitude of the divergence of the $\boldsymbol{\Gamma}^+$-field. The shock strength—and with it the magnitude of the divergence of the $\boldsymbol{\Gamma}^+$-field—varies rapidly along the shock, since the incoming flow is highly non-homogeneous due to the upstream expansion. To account for this variation in weights, the weights were binned based on the x-coordinate and normalized per bin. This yields the following algorithm:

(1) Calculate $\boldsymbol{\Gamma}^+$ characteristics vector field

$$\boldsymbol{\Gamma}^+(\boldsymbol{r}) = \begin{bmatrix} \cos\left(\phi(\boldsymbol{r}) + \mu(\boldsymbol{r})\right) \\ \sin\left(\phi(\boldsymbol{r}) + \mu(\boldsymbol{r})\right) \end{bmatrix}. \tag{8}$$

(2) Calculate $\boldsymbol{F} = \nabla\boldsymbol{\Gamma}^+$ for regions where $M \geq 1$.
(3) Extract $\mathrm{tr}(\boldsymbol{F}) = \nabla \cdot \boldsymbol{\Gamma}^+ < 0$.
(4) Extract from this the subset $\hat{\mathbf{u}} \cdot (\boldsymbol{F}\hat{\mathbf{u}}) < 0$ as the shock region (where $\hat{\mathbf{u}}$ denotes the unit vector in flow direction).
(5) Set the weight to $w = |(\mathrm{tr}(\boldsymbol{F}))| \cdot V_c$, where V_c is the cell volume.
(6) Bin data per x-coordinate and normalize in each bin i the weights by dividing by the maximum weight, i.e.,

$$\hat{w}_{i,j} = \frac{w_{i,j}}{\max\limits_{\text{j in bin i}} (w_{i,j})}.$$

(7) Determine shock line as quartic polynomial regression of z over x weighted with $\hat{w}_{i,j}$.

For shock detection, in general, this procedure should be repeated for the Γ^- characteristics.

3. Riemann solver

The Euler equations can be solved by using a conservative method called approximate Riemann solver,[71] in which Eqs. (2)–(4) are locally diagonalized and split into ordinary differential equations for the fluxes. At each face in a finite volume mesh, the flux is calculated by solving local Riemann problems. An approximate Riemann solver (i.e., dbnsFoam of foam-extend 4.0[42]) with the HLLC (Harten-Lax-van Leer-Contact) scheme[43] is used to calculate the inviscid continuum mechanical solution of the flow field. While approximate Riemann solvers can accurately solve supersonic regions, they possibly give rise to spurious wave modes in the subsonic region,[44] which in the considered flow is the zone between the two jet inlets. A first-order HLLC flux construction was applied to avoid these spurious waves.[45] The temporal discretization is conducted by a fourth-order Runge–Kutta integration, which is explicit and, therefore, required small time steps to maintain numerical stability. A constant time step was chosen, so that the Courant–Friedrichs–Lewy (CFL) number was below 0.3. A solver verification for a shock tube case is presented in Appendix B.

C. Transitional flow regime

In the last decade, multiscale methods have been developed which give promising results at low computational effort for simple rarefied flows, such as the unified gas kinetic scheme,[46,47] discrete unified gas kinetic scheme (DUGKS),[48–50] kinetic relaxation models[51,52] and the general synthetic iterative scheme.[53] Still, the simultaneously ongoing improvements of its algorithm[54] and its inherent numerical stability keep direct simulation Monte Carlo (DSMC)[55] the method of choice for accurate predictions of complex rarefied flows. Therefore, we applied it to study the plume interaction in the transitional flow regime between the two extreme cases of no collisions and local equilibrium. In DSMC, the gas is modeled by the movement and collision of molecules, represented as purely repulsive particles. The particle movement and collisions are decoupled—which mitigates the time step requirement as collisions do not have to be detected during the particle movement. After the movement, the particles are sorted into cells and collide randomly with other particles from the cell. Only the number density in the cell and relative velocity between particle pairs, but not their exact location, determine the collision probability. To further speed up the simulation, one simulation particle represents a large number of real molecules. To obtain accurate results despite these simplifications, the cell size has to be below $1/3\lambda$, the time step size below $1/10\tau$ and the number of particles per cell above 20 (to ensure enough collision partners).[55] We fulfilled the listed resolution criteria in the entire flow field, except for the number of particles in the "blind spot" by which we denote a small region above the inlet with an extremely low number density, so that collisions are improbable.

We used the dsmcFoam+ solver which is part of OpenFoam-2.4-MNF.[56] The collision partners were selected using the No-Time-Counter model. The collisions were calculated using the Variable-Hard-Sphere model.

D. Far-field solution

The far-field solution approximates the number density for continuum flow. It assumes a point source and a decrease in density proportional to the inverse of the distance in radial direction for the two-dimensional case. Hence, in the far-field of a single plume, a self-similar azimuthal density distribution can be assumed. The density distribution can thus be split into a radial and azimuthal function,

$$\frac{n(r,\Theta)}{n^*} = A\frac{R^*}{r}g(\Theta)\,, \tag{9}$$

where A is an integration constant and $R^* = D/2$. For outlet velocities above zero—which will occur due to the high pressure ratio between tank and vacuum—the flow does not spread in all directions at the outlet, but is constrained by the maximum turning angle Θ_{max}. Boynton fitted an azimuthal function to numerical solutions for a three-dimensional plume,[57] which was afterward commonly used. To adapt it for the two-dimensional case, the square-root of this function is considered, which reads

$$g(\Theta) = \left[\cos\left(\frac{\pi}{2}\frac{\Theta}{\Theta_{max}}\right)\right]^{\frac{1}{\gamma-1}}, \tag{10}$$

where for a sonic outlet velocity, as we consider here, the two-dimensional Prandtl–Meyer expansion (PME) defines the maximum turning angle Θ_{max} and maximum velocity U_{max}, which read

$$\Theta_{max} = \frac{\pi}{2}\left(\sqrt{\frac{\gamma+1}{\gamma-1}} - 1\right), \tag{11}$$

$$U_{max} = \sqrt{\frac{\gamma+1}{\gamma-1}}U^*\,. \tag{12}$$

To ensure the mass flux conservation, A is determined by balancing the flux from the orifice with the mass flux integrated over the sphere of a certain radius r_c,

$$n^*U^*2R^* = 2\int_0^{\Theta_{max}} n^*U_{max}\frac{R^*}{r_c}Ag(\Theta)r_c\,\mathrm{d}\Theta\,, \tag{13}$$

which gives

$$A = \frac{U^*/U_{max}}{\displaystyle\int_0^{\Theta_{max}} g(\Theta)\,\mathrm{d}\Theta}\,, \tag{14}$$

which yields $A = 0.572$ for monatomic gas. The approximation tends to be incorrect near the inlet. In addition, the maximum velocity is based on the maximum velocity in a Prandtl–Meyer expansion, but considering that in a free expansion flow all thermal energy is expected to be transferred to kinetic energy, a maximum velocity of $u_{max} = \sqrt{2c_pT_s}$ would be another reasonable estimate.

E. Penetration Knudsen number

To classify the strength of interaction, Koppenwallner[23] (as cited by Dagum and Zhu[24]) introduced the penetration Knudsen number Kn_p as

$$Kn_p(x) = \frac{\lambda_p(x)}{l_{ref}(x)}\,, \tag{15}$$

where λ_p is the mean free path at a position on the symmetry line based on the number density of the far-field solution, and l_{ref} the distance a particle could theoretically penetrate into the other jet from this symmetry line position (see also Fig. 1). Koppenwallner assumed that the lowest penetration Knudsen number $Kn_{p,min}$ is appropriate to classify plume interaction into four different regimes: (1) For a very high minimum penetration Knudsen number, a free molecular flow occurs, and consequently, penetration of molecules from one jet into the other jet; (2) if the mean free path is of the order of the characteristic flow length, collisions between the molecules of the two jets deflect their paths; (3) a further decrease in the penetration Knudsen number ($Kn_{p,min} < 0.2$) yields diffuse shocks slightly before the symmetry plane; after the shock, the flow direction of the molecules nearly aligns with the primary jet axis; and (4) for very small Knudsen numbers ($Kn_{p,min} < 0.02$), a back flow may appear, which could interact with the upstream wall. Other research groups[24–27] used this definition to classify the interaction of plumes: Li and Ladeinde[26] tried to improve the definition by replacing the mean free path based on the number density only, by the one which accounts for the high relative velocity between the two jets. Holz *et al.*[25,68] studied the plume interaction experimentally and confirmed the appropriateness of penetration Knudsen number, which was, however, the more extreme case of $Kn_{p,min} = 0.045$.

Figure 4(a) depicts the minimum penetration Knudsen number $Kn_{p,min}$ map as a function of the inlet Knudsen number Kn_0 and the distance of the inlets for parallel jets. With an increasing inlet Knudsen number, the minimum penetration Knudsen number increases proportionally (the proportionality factor is greater than unity). A higher distance between the jets increases the minimum penetration Knudsen number only marginally, which makes sense considering the estimations $\lambda_p \propto 1/n \propto r$ and $l_{ref} \propto r$ for the two-dimensional case. Figure 4(b) depicts the minimum penetration Knudsen number $Kn_{p,min}$ map as a function of the inlet Knudsen number Kn_0 and the inclination of the inlet streams for a constant inter-jet-distance $l = D/2$ (note that l_{ref} does not only depend on the position of the symmetry line, but also on the jet inclination). When inclining the plumes toward each other—such as in a linear aerospike engine—the penetration Knudsen number is below $Kn_{p,min} = 0.2$ even for high inlet Knudsen numbers, predicting a shock. For plumes inclined away from each other, the penetration Knudsen number rises rapidly, which makes it promising for avoiding shocks and the involved non-uniformities, e.g., in coating deposition.

III. CASE SETUP

A. DSMC boundary conditions

The computational domain and boundary conditions for the DSMC simulation are shown in Fig. 5. To reduce the computational cost, only half of the domain is simulated using the symmetry in the interaction plane to split the domain. The computational domain is of size $L_x = 21$ mm and $L_z = 12$ mm; the inlet of length $D = 3$ mm is positioned at distance L from the symmetry plane, so that $2L$ is the nozzle separation distance.

The assumed stagnation conditions, i.e., the conditions which are in the reservoir upstream the inlet in an experimental setup, are $T_s = 800$ K and varying values for n_s. The sonic inlet conditions are calculated by applying isentropic 1D relations[58]

$$n^* = n_s\left(\frac{\gamma+1}{2}\right)^{\frac{-1}{\gamma-1}}, \tag{16}$$

$$T^* = T_s\left(\frac{\gamma+1}{2}\right)^{-1}, \tag{17}$$

which—with a specific heat ratio $\gamma = 5/3$ and molecular mass $m = 65.38$ u for zinc—yield an inlet temperature $T_{in} = T^* = 600$ K

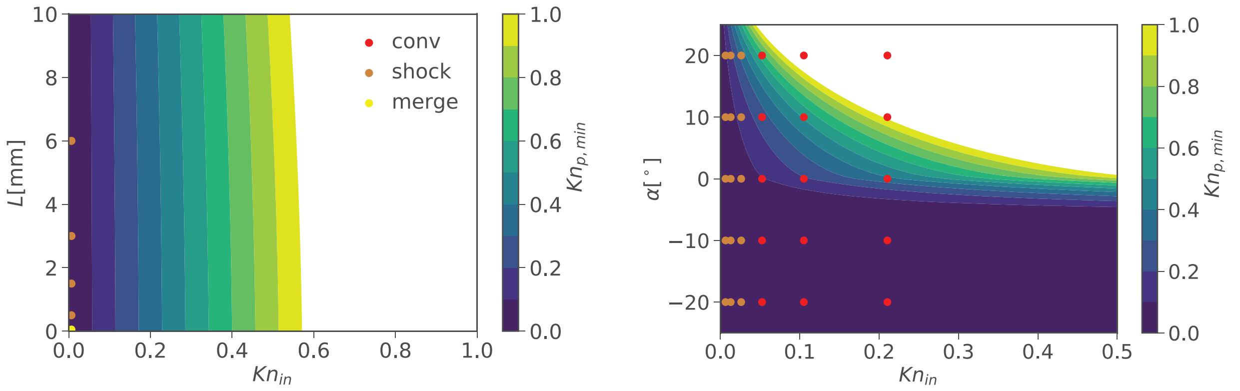

(a) (b)

FIG. 4. Minimum penetration Knudsen number maps (clipped to values below unity); (a) over Kn_{in} and L; (b) over Kn_{in} and α. Simulated cases are marked by points whose color indicates whether a shock ("shock") or only a region of converging Γ^+ characteristics ("conv") could be detected or whether the plumes merge ("merge"). (a) $Kn_{p,min}$ depending on inlet-to-inlet distance L; (b) $Kn_{p,min}$ depending on inlet inclination α.

and an inlet velocity of $u_{in} = a(T^*) = \sqrt{\gamma k_B T^*/m} = 356.56\ \mathrm{ms}^{-1}$. All other boundaries (except for the symmetry) have a vacuum outlet condition for DSMC, i.e., particles are removed from the simulation upon impingement. At the symmetry plane, inciding particles are specularly reflected. Likewise, the walls in the third homogeneous direction of our two-dimensional problem are specularly reflecting.

B. Riemann solver boundary conditions

For the approximate Riemann solver, the outlet is split into a vacuum and a backflow boundary. The supersonic outflow at the vacuum may give rise to numerical shocks possibly distorting the upstream flow field. Hence, a wave-transmissive outlet boundary condition is applied at the vacuum outlets.[59] To stabilize the solution process, the backflow boundary condition was closed during the initialization. In the final solution, the backflow boundary condition distinguishes between outflow and inflow: For outflow, a pressure outlet $p_o = 10^{-5}$ Pa and zero velocity gradient are applied; for inflow, a zero pressure gradient and a zero convective velocity. (The density field is calculated from the ideal gas law.) An overview of the boundary conditions is given in Table I. The discretization and a mesh independence study are presented in Appendix C.

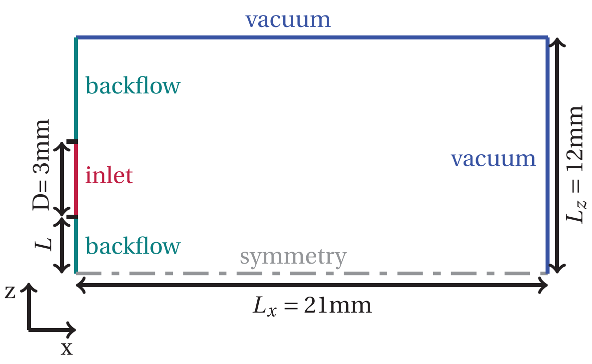

FIG. 5. Geometry and boundary conditions for the DSMC simulation.

C. Zinc vapor properties

As the intended main application is physical vapor deposition, all simulations were conducted for zinc. As the viscosity of zinc vapor has not been studied yet, we applied the inverse-power-law approximation described by Fan *et al.*[60] to approximate the collisional properties. We chose potassium as reference metal, which is in the same group as zinc and whose viscosity is reported in the literature.[61] The approximated Variable-Hard-Sphere collisional diameter of zinc is 5.684×10^{-10} m and the viscosity parameter $\omega = 0.849$ at a reference temperature of $T_{ref} = 2000$ K. The mass of the zinc molecule is set to 65.38 u. For the approximate Riemann solver, only the specific heat at constant pressure is required (as the inviscid equations are calculated), which is for zinc $c_p = 317.901\ \mathrm{J\,kg^{-1}\,K^{-1}}$.

D. Parameter variation

The stagnation Knudsen number describes the rarefaction in the pressure tank upstream of the inlet, which is required to compare to experiments, and reads $Kn_s = \lambda_s/D$, where D is the inlet width and λ_s the Variable-Hard-Sphere mean free path at the inlet, which is

$$\lambda_s = \left(\sqrt{2}\pi n_s d_{ref}^2 \left(\frac{T_{ref}}{T}\right)^{(\omega-1/2)}\right)^{-1}. \tag{18}$$

For easier reference, the cases are addressed as a multiple of the smallest Knudsen number Kn_0. For the present simulations, which start at the inlet, it makes more sense to use the inlet Knudsen number $Kn_{in} = \lambda_{in}/D$. Kn_s can be converted into Kn_{in} using the isentropic relations in Eqs. (16)–(18), which yields

$$Kn_{in} = Kn_s \left(\frac{\gamma+1}{2}\right)^{\frac{1}{\gamma-1}+\frac{1}{2}-\omega}. \tag{19}$$

The rarefaction, distance between the jets, and their inclination away from one another were varied according to Table II. In Fig. 4, the different cases are marked by dots to illustrate the link to the penetration Knudsen number.

TABLE I. Boundary conditions.

		Approximate Riemann solver		
	DSMC	Velocity	Pressure	Temperature
Inlet	n_{in} drawn from Maxwellian with $T_{in} = 600\,\mathrm{K}$ and $u_{in} = 356.56\,\mathrm{ms}^{-1}$	$u_{in} = 356.56\,\mathrm{ms}^{-1}$	p_{in}	$T_{in} = 600\,\mathrm{K}$
Vacuum	Delete particles	Zero gradient	Wave transmissive $p_o = 10^{-5}$ Pa at far distance $l_{inf} = 0.01$ m	Zero gradient
Back flow	Delete particles	If outlet: zero gradient If inlet: $u = \mathbf{0}$	If outlet: $p_o = 10^{-5}$ Pa If inlet: zero gradient	Zero gradient
Symmetry	Reflect particles	Symmetry	Zero gradient	Zero gradient

IV. RESULTS AND DISCUSSION

In the first section of the results, the flow field for collisionless flow is presented for two parallel plumes and the analytical solution is verified (Sec. IV A), followed by the flow field of the Euler equations compared with a rarefied flow field (Sec. IV B). Section IV C shows the characteristics and shock detection for different degrees of rarefaction to visualize the impact of rarefaction on the shock location and understand the flow from another perspective. The last part focuses on the practical application: A comparison of estimated deposition profiles with the DSMC solution (Sec. IV D), an analysis of the impact of nozzle separation distance and tilting on the shock location and deposition (Secs. IV E and IV F), and eventually a discussion of the non-uniformity of the mass flux (Sec. IV G).

A. Collisionless flow field

Figure 6 shows the contours for various flow properties of the collisionless flow ($Kn_s \rightarrow \infty$) for two parallel jets ($\alpha = 0°$) at a nozzle-separation-distance $L = D$. The collisionless DSMC is shown in the upper half and the analytic solution in the lower. They agree well in most regions. In the "blind spot" and far from the inlets, statistical noise begins to show in the DSMC solution due to the small sample size in these highly rarefied regions.

The density normalized by the inlet density decreases behind the outlets [Fig. 6(a)]. Around the symmetry plane, the superposition of the plumes produces an increased density. The velocity magnitude, shown in Fig. 6(b), increases downstream of the inlets due to "sorting" of the particles according to their velocity: While initially directed in several directions, particles align with the mean velocity the farther they travel away from the inlet. Therefore, the particles' velocities contribute increasingly to the mean velocity and decreasingly to the temperature. However, between the plumes the two fluxes from the inlets are counterdirected and the mean velocity cancels out yielding a low velocity region. The velocity sorting produces a low temperature in regions of high alignment between the particles' velocities and the mean velocity, e.g., in the expansions, as shown in Fig. 6(c). Between the two plumes, where the mean velocity cancels out, the immense relative velocities give a huge variance of particle velocities, and consequently a high temperature—even higher than at the inlet. The Mach number, shown in Fig. 6(d), depends strongly on the sorting of velocities, since both the velocity and the speed of sound ($a \propto \sqrt{T}$) are affected. The Mach number increases in the far-field to a value around $M = 1.8$. In the near-field of the flow, where a low velocity and high temperature prevail, a subsonic region occurs around the symmetry plane.

TABLE II. Variation parameters: rarefaction Kn_s and corresponding inlet conditions, nozzle separation distance L, and inlet inclination α. (p_{in} is only listed for cases which were calculated with the approximate Riemann solver.)

Kn_s	Kn_{in}	$n_{in}\left[\frac{10^{20}}{\mathrm{m}^3}\right]$	p_{in} (Pa)	L	α (deg)
$Kn_0 = 0.0047$	0.0066	232.09	192.264	$D/60$	−20
$2Kn_0 = 0.0095$	0.0132	116.05	96.132	$D/6$	−10
$4Kn_0 = 0.0189$	0.0263	58.02	⋯	$D/2$	0
$8Kn_0 = 0.0378$	0.0526	29.01	24.033	D	10
$16Kn_0 = 0.0756$	0.1052	14.51	⋯	$2D$	20
$32Kn_0 = 0.1512$	0.2105	7.26	⋯		
$64Kn_0 = 0.3024$	0.4209	3.63	⋯		

B. Continuum flow and transitional flow regime

The upper half of Fig. 7 shows the flow field of two interacting plumes at $Kn_S = 2Kn_0$ ($L = D$, $\alpha = 0°$) solved by the approximate Riemann solver for the inviscid Euler equations. As in the collisionless case, the flow expands downstream from the inlet. Density, temperature and pressure decrease, whereas the velocity increases with increasing distance from the inlet. The isolines form ellipses, that are symmetric about the jet axis, which implies that the primary expansion is well protected against any influence from the other jet. The temperature drops to a lower level than for collisionless flow, tending toward zero; and the velocity rises higher, with values above $U = 600\,\mathrm{ms}^{-1}$. Both phenomena are caused by an expansion which is not diffuse as in the collisionless case, but directed by the pressure gradient which in the presence of collisions efficiently transforms thermal energy into kinetic energy. Please note that thermal energy is also transferred from the homogeneous direction (i.e., here the y-direction) into kinetic energy in the planar flow plane thus enhancing the acceleration, which is impossible in collisionless flow. Around the symmetry plane a sharp discontinuity occurs for all flow variables. Density and temperature rise, the velocity drops. The discontinuity traverses through the entire flow field in a shape similar to a Laval nozzle. The flow variable

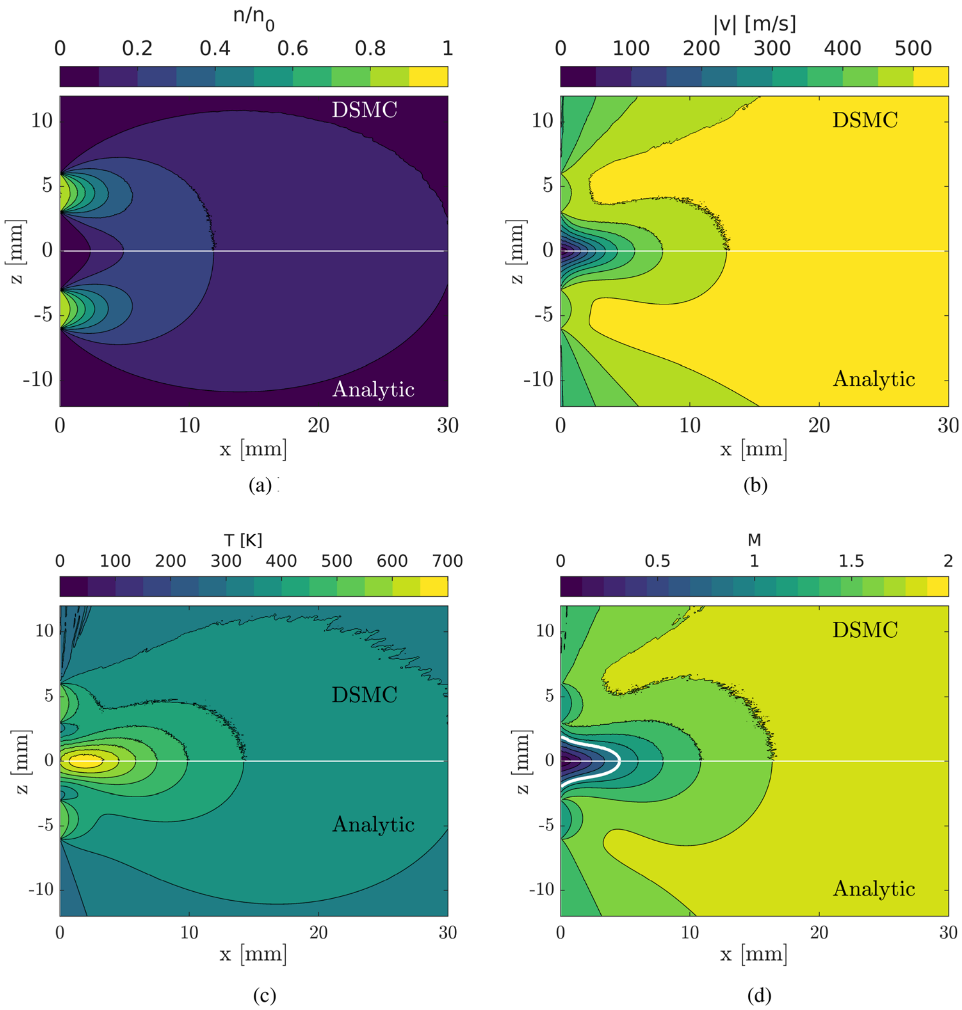

FIG. 6. Flow field contours of collisionless flow ($Kn_s \rightarrow \infty$) for two parallel ($\alpha = 0^\circ$) plumes at a nozzle-separation-distance $L = D$: (a) density, (b) velocity magnitude, (c) temperature, and (d) Mach number. The upper half shows the DSMC solution and the lower half the analytic solution.

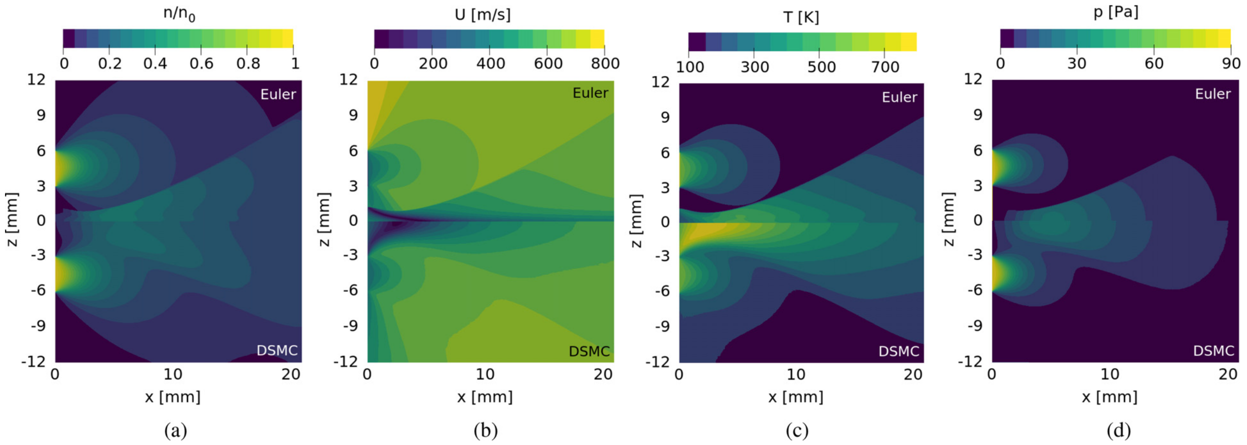

FIG. 7. Flow field contours of two parallel $\alpha = 0^\circ$ interacting plumes at a nozzle-separation-distance $L = D$ for a stagnation Knudsen number of $Kn_s = 2Kn_0$: (a) density, (b) velocity magnitude, (c) temperature, and (d) pressure.

extrema in the inter-shock region are close to the "throat" (i.e., the narrowest section), and from there they mitigate in both directions, i.e., in the back flow and the so-called secondary expansion. The temperature values are highest next to the symmetry plane, which increases the pressure; this in turn will keep the number density in the center of the inter-shock region lower than near the shocks.

The lower half of Fig. 7 shows the flow field of same two interacting plumes ($L = D, \alpha = 0^\circ$, $Kn_S = 2Kn_0$) solved by DSMC. The flow exhibits a higher similarity with the continuum case in the upper half of Fig. 7 than the collisionless case (Fig. 6), since its rarefaction is low. However, the shielding of the shock does not hold anymore, and the high number density of the inter-shock region diffuses into the primary expansion. The increase in velocity and decrease in temperature are mitigated, as missing collisions imply less efficient transfer of thermal energy to macroscopic kinetic energy. This entails a delayed expansion as can be observed in the velocity contours. In the inter-shock region, the temperature exceeds both the collisionless and the continuum flow. While the shock—typical of low rarefaction—accumulates the energy behind the shock, the diffuse behavior due to rarefaction keeps more energy in the thermal than in the macroscopic kinetic mode. The higher temperature increases the effect of keeping the number density around the symmetry plane lower than directly behind the shocks. The shock location—which for continuum flow was obvious and consistent between all contours—is not clearly determinable for the rarefied solution, which is why we use the MOC to identify the shock location in Sec. IV C.

C. Visualization by method of characteristics

Visualization by the Method of Characteristics shifts the view from the descriptive character of the macroscopic thermodynamic properties to the hyperbolic character, which determines the inviscid continuum flow behavior and to a large extent still the one in the transitional flow regime for the considered case, since a sufficient number of collisions occurs in crucial parts, such as the inlet region and the shock to approach continuum flow behavior (from a large-scale point of view). Figure 8 depicts the characteristics of the flow fields as well as the detected shock region in continuous blue contours; the gray, banded contours in the background represent the Mach number. Figure 8(a) shows the inviscid continuum case (with an inlet density based on $Kn_s = 2Kn_0$) in the upper half and the corresponding DSMC solution in the lower half. For the inviscid continuum case, the Γ^- expansion fan unfolds around the upper corner of the inlet, the Γ^+ expansion fan around the lower corner. When crossing each other, their interaction causes the characteristics to bend slightly. The streamlines, depicted in blue, run along the half angles. In the shock,

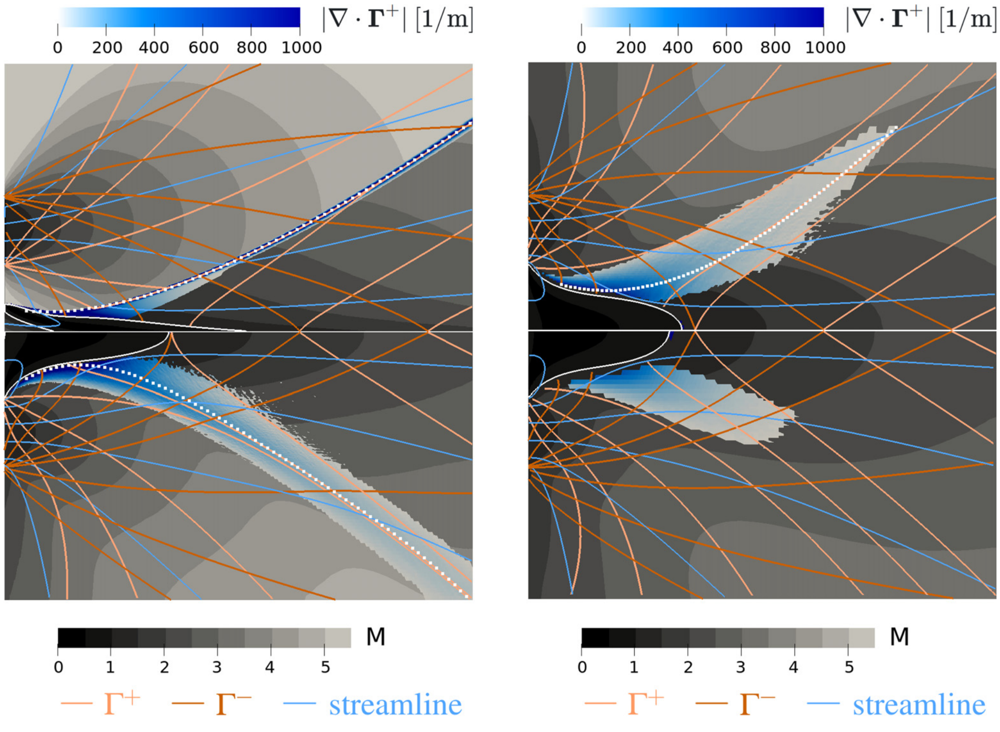

(a) (b)

FIG. 8. Characteristics and shock detection (a) for $Kn_s = 2Kn_0$, in the upper half the Euler solution is shown, in the lower half the DSMC, (b) for DSMC solutions for $Kn_s = 4Kn_0$ in the upper half and $Kn_s = 8Kn_0$ in the lower half. The gray, banded contours in the background show the Mach number; the blue, continuous contours represent the region detected as shock region and are colored by $|\nabla \cdot \Gamma^+|$, clipped at 1000 m^{-1}. The blue lines are streamlines, the brown lines Γ^- characteristics, and the beige lines Γ^+ characteristics (in the lower part the characteristics are mirrored). The white dotted line is the shock line detected from the regression of the shock region; the white solid line is the sonic line, i.e., $M = 1$. (a) $Kn_s = 2Kn_0$. The upper half depicts the Euler solution, the lower half the DSMC solution. (b) The upper half depicts the DSMC solution for $Kn_s = 4Kn_0$, and the lower half the DSMC solution for $Kn_s = 8Kn_0$.

the Γ^+ characteristics turn sharply and merge with the shock, while the Γ^- characteristics cross the shock with only marginal bending. The streamlines turn accordingly. Upon impingement on the subsonic region or the symmetry, the Γ^- characteristics are reflected and turn into Γ^+ characteristics. Initially the reflection angle is wide and the post-shock Γ^+ characteristics hit the shock from downstream and thus bend it upward. However, further downstream the Γ^+ characteristics are parallel to the shock or tend already away from it and so will not hit it and bend it further.

In the following discussion of the transitional flow regime, please keep in mind that with rarefaction the characteristics lose their ability to exactly describe the mechanisms determining the local solution. Yet the qualitatively similar flow behavior allows a meaningful visualization using the characteristics. For the DSMC solution of the $Kn_s = 2Kn_0$ case [Fig. 8(a) lower half], the Γ^+ characteristics exhibit a pattern comparable to the Euler solution, but bend earlier and more smoothly, merging gradually with the shock. The subsonic region is bigger reaching to the corners of the inlet and, in particular, exhibits a bigger concave region, from which the shock region starts. The shock region passes the computational domain at a rather constant, large width. However, the $|\nabla \cdot \Gamma^+|$ values are lower than for the continuum case and rapidly decrease when passing through the domain. Even when considering its broad domain, the shock region distinctly bends more outward than in the Euler solution. So the secondary expansion is wider, but the increase in Mach number is less steep, which would be a contradiction in pure inviscid continuum flow. The underlying reason is that the secondary expansion maintains a higher pressure, temperature and hence speed of sound in the transitional flow regime (refer to Fig. 7). On the one hand, the information that there is a shock travels further upstream due to the higher speed of sound (another equivalent line of argument is that the expansion experiences the shock, when its pressure is equal to the one behind the shock, which happens earlier for higher pressures in the secondary expansion). On the other hand, the high thermal fraction of energy leaves less for the macroscopic kinetic energy which in combination with the high temperature gives a lower Mach number. Appendix D compares the shock structure with the detected shock location to validate the applied shock detection method.

Figure 8(b) shows the DSMC solution for $Kn_s = 4Kn_0$ in the upper and the one for $Kn_s = 8Kn_0$ in the lower half. With increasing rarefaction, the Mach number rises more slowly in the expansions, as fewer collisions transfer thermal energy into macroscopic kinetic energy. For a low number density, the characteristics bend more, especially in the “blind spot.” The Γ^+ characteristics bend well before the shock region aligning gradually with the shock. Consequently, the shock region is much broader than for $Kn_s = 2Kn_0$, but the strength of the divergence $|\nabla \cdot \Gamma^+|$ is lower. The shock does not pass through the entire domain, but dissolves earlier. At $Kn_s = 8Kn_0$, the shock region is even smaller and a detection of a shock line is not feasible anymore.

Figure 9 compares the shock location and sonic line for several degrees of rarefaction. For higher degrees of rarefaction, the subsonic region becomes thicker (i.e., it extends more into the primary expansion) and shorter, indicating an earlier rise of velocity due to an earlier onset of expansion. This agrees with the shift of shock line, which moderately shifts upstream for higher rarefaction.

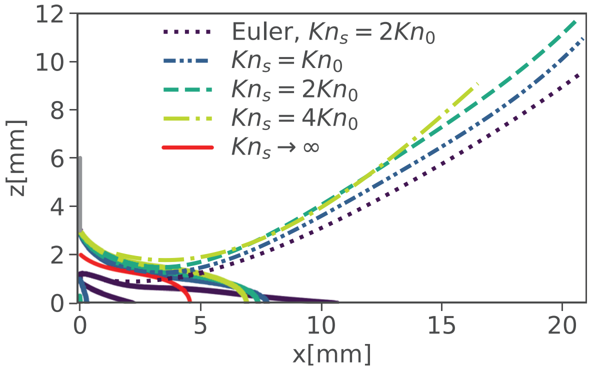

FIG. 9. Shock location (dashed or dotted line) and sonic lines (solid) for different degrees of rarefaction. The vertical gray line denotes the inlet, the red dots the sonic line for free molecular flow.

D. Deposition profiles

After the location detection of the shock, its impact on the deposition is quantified. To this end, Fig. 10 compares the profiles for different solutions methods. Both the free molecular solution and the far-field approximation are superpositions of two single plumes and exhibit two peaks in number density around the inlet positions [Fig. 10(a)]. The far-field approximation is in reasonable agreement with the Riemann solution outside the interaction region. Between the inlet peaks, the far-field approximation predicts a smooth uniform plateau, whereas the inviscid Euler solution produces symmetric profiles about the inlet axis, which means that the plumes are shielded from each other. However, two sharp peaks occur close to the symmetry plane marking the shock locations with high density accumulation in between. Compared to the approximations, the number density of the transitional flow regime is qualitatively a blending [Fig. 10(d)]: At a low Knudsen number, the impact of the shock is severe and the profile resembles the Riemann solution, but with higher peaks and a deeper trough in between. This may be explained with the higher temperature and consequently higher pressure at the symmetry plane [refer to Figs. 7(c) and 7(d)], which deters particles from the symmetry. With increasing rarefaction, the density peak due to the shock diminishes and the rise due to the shock becomes less sharp. The spread outside the interaction region remains similar to those of the far-field and continuum solutions, as it is determined by the collisions right after the inlets, which still play a major role for the degrees of rarefaction considered.

The axial velocity outside the shock region is higher for the continuum flow than for the free molecular one [Fig. 10(b)], as in continuum the temperature is actively transformed into kinetic energy, while in free molecular flow the energy transfer from thermal to kinetic energy is caused by particle velocity sorting which is diffuse and not targeted. In the shock region, velocity drops severely for the continuum solution. The velocity profile in the transitional flow regime [Fig. 10(e)] is as smooth as the free molecular one, but reaches a maximum velocity as high as the continuum flow (since the collisions after the inlet are responsible for accelerating the flow), and rather small values around the symmetry plane (since there are still enough collisions to form a shock).

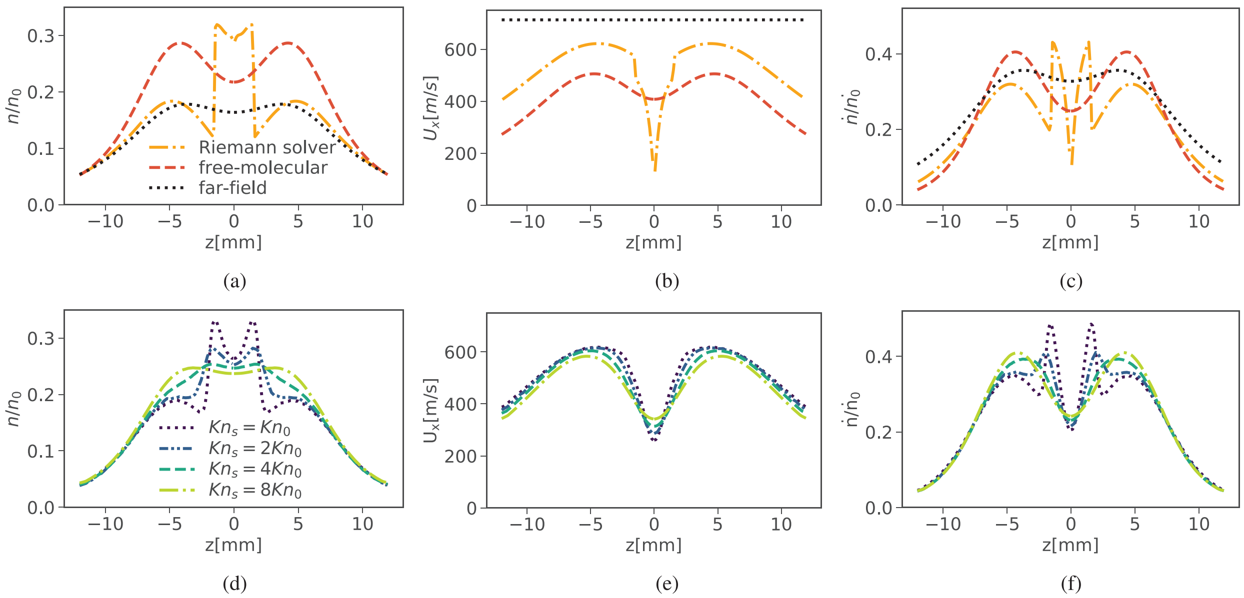

FIG. 10. Profiles of normalized number density, velocity in x-direction, and normalized deposition rate at $x = 6$ mm for the inviscid continuum flow (Riemann solver, inlet density corresponds to $Kn_s = Kn_0$), free molecular flow and the far-field approximation [(a)–(c)] and in the transitional flow regime (DSMC) at different degrees of rarefaction [(d)–(f)]. (a) Normalized number density, (b) x-component of velocity, (c) normalized deposition rate, (d) normalized number density, (e) x-component of velocity, and (f) normalized deposition rate.

The deposition profile is estimated as the product of number density and axial mean velocity (for perfect sticking the actual deposition could deviate marginally due to velocity fluctuations, i.e., temperature). As the peak in density coincides with the trough in velocity, the deposition profiles have a higher agreement for different methods and degrees of rarefaction than the density profiles. When comparing the deposition profile, it is striking that the peaks for the lowest rarefaction in Fig. 10(f) exceed the ones in the Riemann solution in Fig. 10(c) by approximately 10%. The reason is that due to the diffusive nature in the transitional flow regime the density rises in a region where the velocity is still high, whereas the sharp discontinuity in continuum flow keeps high density and high velocity regions distinctly apart. (Consequently, the peaks in deposition are marginally shifted outside compared to the peaks in number density.)

The temperature for the continuum solution is about three times lower than the inlet temperature outside the shock region [Fig. 11(a)]. The temperature peak inside the shock region is as high as the inlet temperature. For free molecular flow, the temperature is approximately one half of the inlet temperature, except for the region around the symmetry plane where it peaks at a modest level. The high temperature for free molecular flow is the counterpart to its low velocity, both stemming from the diffuse distribution of translational energy in the absence of collisions. In the transitional flow regime, the temperature profile [Fig. 11(b)] has a shape between those of continuum flow and free molecular flow, but its peak temperature surpasses theirs, because the high energy accumulation inside the shock as seen in the continuum flow interferes with the diffuse movement of particles typical of transitional flow. This higher temperature is responsible for the deeper trough in number density at the symmetry plane. Despite the described differences between the Riemann solver solution for the Euler equations and the DSMC solution, the Riemann solver gives an estimate of local deposition rates within engineering precision (≈10%) for very low Knudsen numbers, such as $Kn_s = Kn_0$, whereas the free molecular solution fulfills this for $Kn_s > 8Kn_0$. In between these

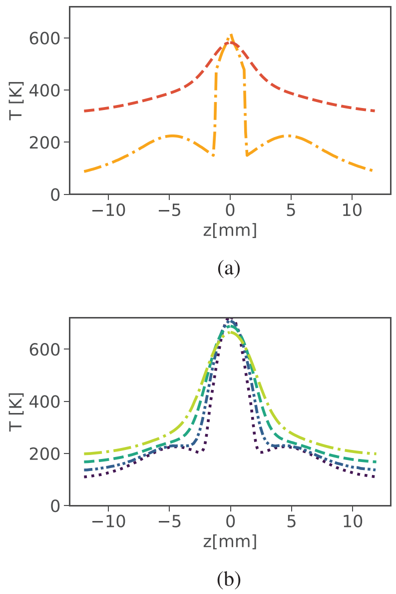

FIG. 11. Temperature profiles for (a) inviscid continuum flow (Riemann solver) and free molecular flow; (b) for the transitional flow regime (DSMC) at different degrees of rarefaction.

Knudsen numbers, DSMC is required to accurately predict the impact of the interaction. We hypothesize that the validity range of the Riemann solution could be enlarged by solving the Navier–Stokes–Fourier equations rather than the Euler equations. This would add the diffusive character due to viscosity (which increases with temperature and independent of other variables, such as density[62]), but not the one due to rarefaction (which is expected to be considerably higher). However, further research is needed to test this hypothesis.

E. Distance

Figure 12 shows the subsonic region and shock location [Fig. 12(a)] and number density contours [Figs. 12(b)–12(f)] for different distances between the inlets. For higher nozzle separation distances, the shock line smoothly follows the concave part of the subsonic region, before it turns away due to the expansion. The smaller the nozzle separation distance, the smaller and more convex the subsonic region. The shock wave strongly bends away from the symmetry line for $L = D/6$. This is caused by the high mass flow into the subsonic region and across the shock which forces a higher pressure in the secondary plume which results in a strong expansion. For the even smaller nozzle separation distance of $L = D/60$, the subsonic bubble has a maximum half height of 0.02 mm or about 10 times the local mean free path. The jets merge and no shock is detectable anymore. The shock does not disappear for high nozzle separation distances (at least in the considered range)—which is in agreement with the discussion of the penetration Knudsen number for planar plumes in Sec. II E, but its impact on the deposition changes. Figure 12(g) plots the deposition profile at $x = 9$ mm for different nozzle separation distances. For $L = D/60$, only one peak is visible, which splits into two for $L = D/6$. For higher distances, the peaks from the primary plumes and the interaction shocks become distinguishable. While at a high nozzle separation distance of $L = 2D$, the peaks due to the shock are similar to the peaks from the primary expansions, the non-uniformity is still high and the deposition per length is small.

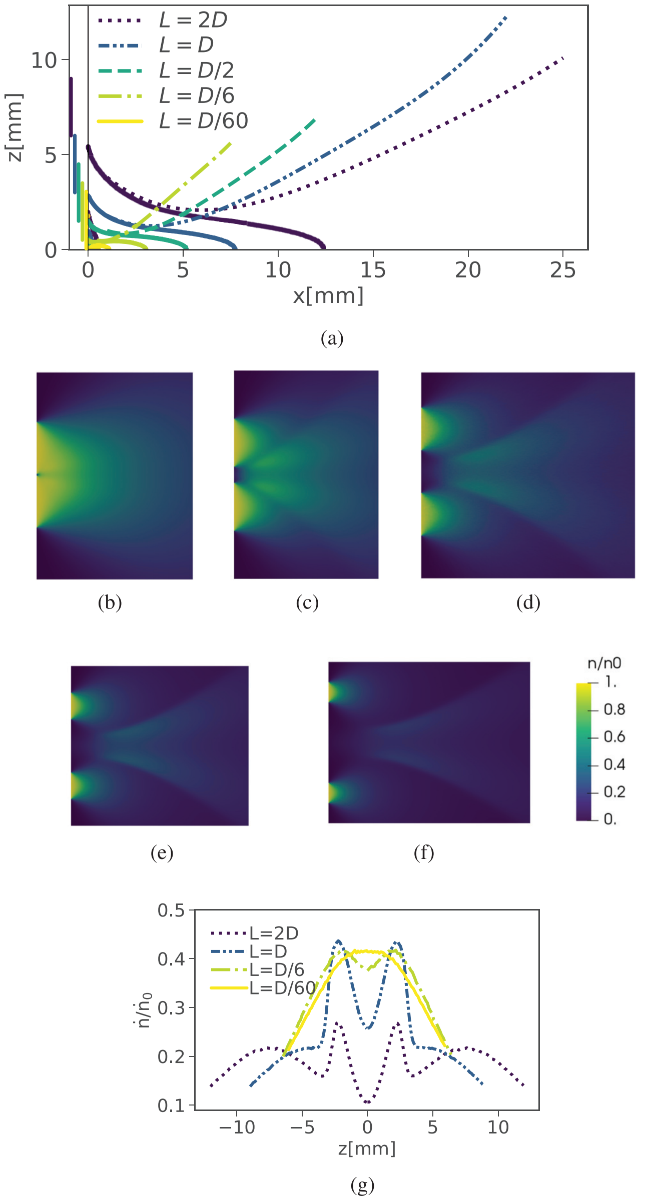

FIG. 12. Influence of nozzle separation distance for parallel plumes at $Kn_s = Kn_0$. (a) Comparison of shock locations, (b)–(f) number density contours, (g) deposition profile. (a) Shock location (dashed or dotted lines) and sonic line (solid) for different nozzle separation distances. The vertical solid lines on the left mark the inlet location. (b) $L = D/60$, (c) $L = D/6$, (d) $L = D/2$, (e) $L = D$, (f) $L = 2D$, and (g) normalized deposition rate at $x = 9$ mm.

F. Tilting

Figure 13(a) shows the shock location and sonic line for several jet inclinations. Tilting the jets more toward each other (i.e., $\alpha = -10°$ and $\alpha = -20°$) reduces the subsonic region. It does not extend that far into the primary plume, as the high density caused by tilting it toward the symmetry plane shields the first plume from particles penetrating from the other primary plume. On the other hand, the high number density crossing the shock increases the pressure after the shock, which drives the secondary expansion, thus enforcing the latter. Consequently, the expansion bends the shock line more away from the symmetry plane and the flow expands faster, producing a smaller subsonic region. (The same phenomenon can also be explained in terms of characteristics: as the expansion fan from the inlet is more inclined toward the symmetry plane, the reflected Γ^+ characteristics impinge onto the shock at wider angles and thus cause a stronger expansion. Consequently, the shock bends more away from the symmetry plane.) By tilting the inlet streams away from each other (i.e., $\alpha = 10°$ and $\alpha = 20°$), the opposite effect occurs. The subsonic region starts slightly further upstream, fewer particles cross the shock producing a weaker secondary expansion. For the inclinations and Knudsen numbers under consideration, it was decided based on the detected shock region, whether it is feasible to draw a shock line or whether the region can be neglected as a compression region not strong enough to cause a shock. The results are marked in Fig. 4(b). Independent of the inclination of the jets, a shock was detected for stagnation Knudsen numbers up to $4Kn_0$; above $8Kn_0$, only a compression region emerged around the subsonic region. However, the deposition profiles do depend on the inclination.

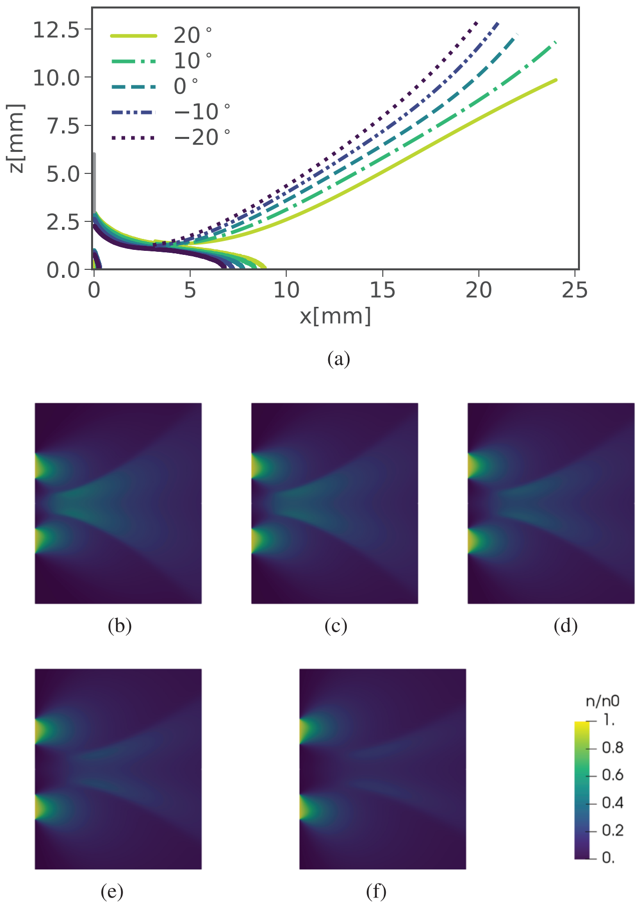

(a)

(b) (c) (d)

(e) (f)

FIG. 13. Influence of tilting the inlet velocity ($Kn_s = Kn_0$ and $L = D$). (a) Comparison of shock location and subsonic region, (b)–(f) number density for several degrees of inclination. (a) Shock location (dashed or dotted lines) and sonic line (solid) for different angles of tilting of the inlet velocity, (b) $\alpha = -20°$, (c) $\alpha = -10°$, (d) $\alpha = 0°$, (e) $\alpha = 10°$, and (f) $\alpha = 20°$.

Figure 14 shows the profiles for the number density, normalized by the inlet density, the velocity component parallel to the jet axis, and the deposition rate normalized by the inlet flow rate over the z-coordinate at $x = 6\,\text{mm}$ [Figs. 14(a)–14(c)] and $x = 15\,\text{mm}$ [Figs. 14(d)–14(f)] at $Kn_S = Kn_0$ for different inclination angles. At $x = 6\,\text{mm}$, the shock is at the same position for the different inclinations [Fig. 13(a)], which is reflected by the same location of the two peaks in the density profile. However, the height of these peaks is negligible for $\alpha = 20°$ and immense for $\alpha = -20°$, as with the latter a much higher number density flux already crossed the shock. The velocity profiles [Fig. 14(b)] at this position approximately match for the different inclinations and exhibit a low value in the shock region, which mitigates the impact of the shock in the deposition profile [Fig. 14(c)]. Further downstream, at $x = 15\,\text{mm}$, the two broad peaks from the shocks dominate the density profile [Fig. 14(d)]. They have a similar maximum value, but the stronger expansion for cases inclined toward each other broadened the peaks farther over the domain. In addition, the density trough around the symmetry is smaller yielding a flatter, more uniform density profile than for plume inclinations away from the symmetry. The velocity profiles [Fig. 14(e)] resemble each other in shape with an undisturbed accelerated flow at the edges of the domain, a small trough at the start of the shock, and a deeper one in the center. The main difference between the inclinations being that for plumes inclined to each other the low Mach number region between the shocks extends farther and the expansion already began, which reaccelerates the flow between the shocks and mitigates the velocity trough in the center. The overall deposition [Fig. 14(f)] in the depicted segment is considerably higher for plumes tilted toward each other, since less mass flow leaves the domain. This reduction in stray deposition is a desirable side effect for coating technology. The non-uniformity in the deposition rate profile is mitigated compared to the upstream profile. This applies in particular, to $\alpha = -20°$, which had (perceptibly) the highest deposition non-uniformity at $x = 6\,\text{mm}$ and the lowest at $x = 15\,\text{mm}$. To provide a more general overview of non-uniformity, we quantify it in Sec. IV G.

G. Deposition uniformity

A major objective was to determine the effect of nozzle tilting and rarefaction on the uniformity of the deposition. While small variations in coating thickness may be tolerable, strong deviations should be avoided. Based on this consideration, we chose the minimum square deviation from a constant height c as a measure of non-uniformity,

$$A_{dev} = \min_{c\in\mathbb{R}} \int_{z=0}^{z_{60\%}} \left(\frac{\dot{n} - c}{c}\right)^2 \mathrm{d}x\,, \tag{20}$$

where $z_{60\%}$ is the position where 60% of the influx would be deposited. The choice of such a cutoff coordinate is required to exclude the long thin tail of deposition (which can also not be captured by the finite computational domain). For a perfectly uniform deposition, $A_{dev} = 0$; the stronger and more numerous the deviations, the higher A_{dev}. Figure 15 plots A_{dev} over different degrees of rarefaction and nozzle-to-plate distances, using a logarithmic scale. For very short nozzle-to-plate distances, the non-uniformity is high and nearly independent of the rarefaction, since it captures the non-uniformity from the two jet inlets only. Non-uniformity decreases with the distance to the inlets. A strong mitigating effect of rarefaction sets in around $x = 6\,\text{mm}$, which corresponds to the start of the shock. For high rarefaction equal to or greater than $Kn_s = 16Kn_0$ and for free molecular flow, the minimum non-uniformity is reached around $x = 12\,\text{mm}$ and increasing again afterward. While the two plumes superposed each other before, they merge into one single plume further downstream, which increases non-uniformity. For lower rarefaction (i.e., equal to and below $Kn_s = 8Kn_0$), non-uniformity monotonically decreases with the distance to the inlet (for the region considered), thus exhibiting lower non-uniformity at high distances than the higher rarefied cases. This is the result of the interaction shock which "fills" the trough between the two primary plumes, producing a broad plateau in the deposition profile. When the jets are tilted toward each other [Fig. 15(b)], the non-uniformity decreases faster with increasing distance from the inlet. The minimum for free molecular flow is reached closer to the inlet than for parallel jets, since the density peaks merge earlier to form a plateau and then a single density peak. For long distances from the

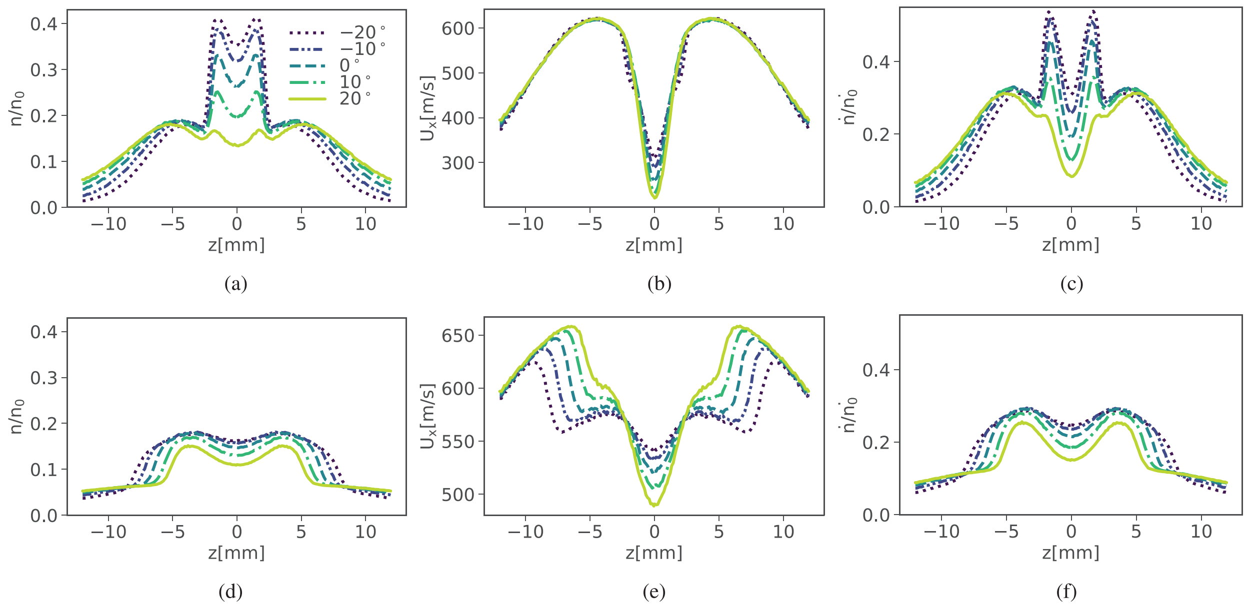

(a) (b) (c)

(d) (e) (f)

FIG. 14. Normalized density, Mach number, and normalized deposition profiles for several inclination angles (a)–(c) at $x = 6$ mm and (d)–(f) at $x = 15$ mm. (a) Normalized number density at $x = 6$ mm, (b) Mach number at $x = 6$ mm, (c) normalized deposition rate at $x = 6$ mm, (d) normalized number density at $x = 15$ mm, (e) Mach number at $x = 15$ mm, and (f) normalized deposition rate at $x = 15$ mm.

inlet, the minimum occurs for a rarefaction of $Kn_s = 4Kn_0$ compared to $Kn_s = 8Kn_0$ for the non-inclined case.

V. CONCLUSIONS

We have investigated the interaction of two sonic, rarefied, planar plumes—either parallel or inclined to each other. The extreme cases of a collisionless analytic flow solution and an inviscid continuum solution calculated by an approximate Riemann-solver were presented. In the transitional flow regime, multiple DSMC simulations were conducted. To analyze the flow field, we detected the characteristics and used their divergence to detect the shock location.

For free molecular flow, the expansion stems purely from the sorting of the particles' velocities, producing only a moderate increase in velocity and a small decrease in temperature compared to collisional flow. The inviscid continuum solution gives strong expansions, with rapid increases in velocity and drops of density and temperature. The interaction causes sharp shocks passing through the flow domain, which is reflected in two severe peaks in the deposition profile. Common to both flow regimes is a high temperature in the symmetry plane. The behavior in the transitional flow regime is a blend of free molecular flow and continuum flow. However, some flow variables and fluxes lie outside the limits of these two extreme cases. In and behind the subsonic region, the temperatures exceed both the free molecular and the continuum solution. On the one hand, this results from the high particles and thus energy accumulation, due to the shock which is typical of continuum/collisional flow; on the other hand, a lack of collisions compared to the continuum case enables diffuse particle movement and hinders the energy transfer from temperature to macroscopic kinetic energy. The latter phenomenon yields a wider, but less strong secondary expansion bending the interaction shocks apart. The mass flux peak values in the transitional flow regime exceed the one of continuum flow.

A shock can be perceived up to very small nozzle separation distances. Only when the distance is of the order of $\mathcal{O}(10)$ mean free paths or less, a shock region cannot be detected anymore and the two plumes merge into one single plume. Tilting the plumes toward each other shifts the onset of the shock further upstream and as a result of the higher flux crossing the shock enhances the secondary expansion compared with parallel plumes. This causes steep density peaks at small distances from the inlet. Conversely, the increased pressure enhances the expansion, resulting further downstream in a more homogeneous density and mass flux, while decreasing stray deposition. The non-uniformity in the deposition decreases with distance from the inlets for high rarefaction, and minimizes approximately at the coordinate, where the subsonic region ends. When inclining the plumes toward each other, the distance, at which the minimum non-uniformity is reached, decreases.

Our findings can support the design of vacuum technology, such as physical vapor deposition, to obtain homogeneous mass, momentum and energy fluxes. In addition, they may help in analyzing backflows of multithrusters and their potential structural damage on space vehicles, such as micro-satellites.

We studied the planar case of interacting plumes, which in the broadest sense is representative of linear aerospike nozzles. Especially in aerospace applications, three-dimensional clusters are common, the simulation of which involves significantly higher computational costs for a well-resolved DSMC. For three-dimensional plume clusters, a mitigation of shock effects is expected, as the gas can escape the shock

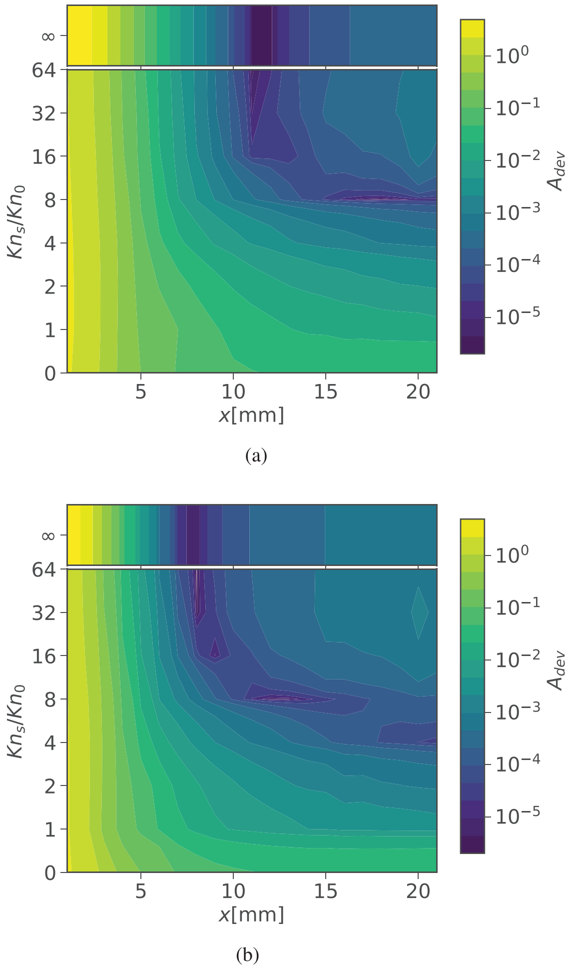

(a)

(b)

FIG. 15. Non-uniformity A_{dev} over different degrees of rarefaction and nozzle-to-plate distances for two (a) parallel and (b) inclined jets at a nozzle separation distance $L = D$. The inlet number density for the inviscid continuum solution at $Kn_s = 0$ is the one for $Kn_s = Kn_0$. The free molecular solution is kept separate. The underlying grid of the contour plot is 20 × 8. (a) Parallel jets, i.e., $\alpha = 0°$. (b) Jets inclined by $\alpha = -20°$.

region in another direction, while for three-dimensional toroidal aerospikes[63] an increase in the shock effect is expected, since a higher mass flux enters the interaction region.

ACKNOWLEDGMENTS

We would like to thank Dr. Ferry Schrijer and Professor Stefan Hickel for an insightful discussion on the Method of Characteristics. This research was carried out under Project No. F22.3.13512 within the framework of the Industrial Partnership Program of the Materials innovation institute M2i (www.m2i.nl) and the Foundation for Fundamental Research on Matter (FOM), which is part of the Dutch Research Council (NWO). The computations were carried out on the Dutch national e-infrastructure with the support of SURF Cooperative.

APPENDIX A: EQUATIONS FOR COLLISIONLESS FLOW SOLUTION

The velocity $\boldsymbol{\xi}$ of each particle is split into a local mean velocity $\mathbf{u}$ and a fluctuational velocity $\mathbf{c}$, i.e., $\boldsymbol{\xi} = \mathbf{u} + \mathbf{c}$. Equilibrium and a non-zero mean velocity are assumed to prevail at the outlets of the nozzles, so that the particle velocity distribution results from a Maxwellian distribution $f_0(\mathbf{c})$ shifted by the mean inlet velocity $\mathbf{U_0}$. For each point in the flow domain, Cai and Boyd[34] integrated the moments over a region in velocity space bounded by the velocity vectors, for which particles leaving from the two utmost points of the inlet reach the studied point (the corresponding bounding vectors are **a** and **b** in Fig. 16). For a planar, sonic, non-inclined jet, the moment $M_\Psi \in [n, v_x, v_z, e]$ of an invariant $\Psi \in [1, \xi_x, \xi_z, 1/2\mathbf{c}^2]$ can be obtained by integrating over the invariant weighted with the phase density, which gives

$$M_\Psi(\mathbf{r}) = \iiint_\Omega \Psi f_0(\mathbf{c})\, \mathrm{d}\mathbf{c}\,, \tag{A1}$$

where the kinematic relation

$$\Omega : \frac{z - \frac{D}{2}}{x} < \frac{c_z}{c_x + U_0} < \frac{z + \frac{D}{2}}{x} \tag{A2}$$

bounds the integration over velocity space to those velocities which may reach the point $\mathbf{r}$. The corresponding domain is shown in Fig. 16 on the right. Cai and Boyd transformed the integration domain over the velocity space to polar coordinates with the velocity magnitude $|\boldsymbol{V}| = \sqrt{(U_0 + c_x)^2 + c_z^2}$ as the radial component and the angle Θ which is formed by the jet axis and the vector connecting the studied point with a point on the inlet boundary, as the angular component. The corresponding integration element is $\mathrm{d}\xi = |\mathbf{V}|\mathrm{d}|\mathbf{V}|\,\mathrm{d}\Theta$. The transformed integration reads as

$$M_\Psi(\mathbf{r}) = \iiint_\Omega \Psi f_0(\boldsymbol{\xi})\, |\mathbf{V}|\mathrm{d}|\mathbf{V}|\mathrm{d}\Theta\,, \tag{A3}$$

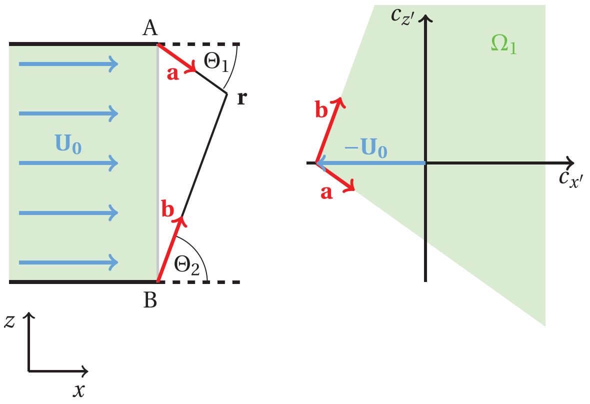

FIG. 16. Single straight jet. On the left, there is a sketch of the jet geometry in real space, on the right the velocity domain as introduced by Cai and Boyd.[34] To obtain the solution at point **r**, the velocity space is integrated over the region bounded by vectors *a* and *b* which connect the outlet with point **r**.

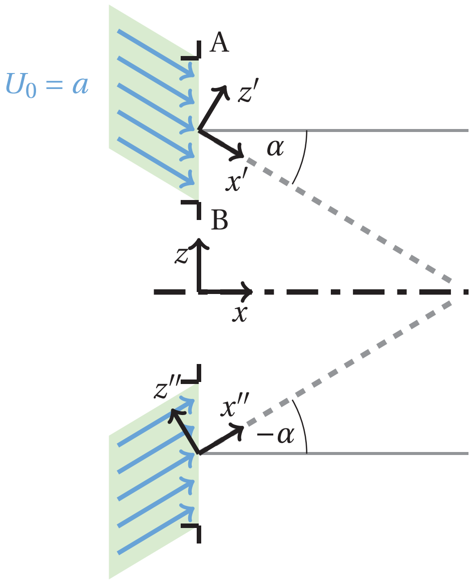

FIG. 17. Coordinate transformation for jets inclined at angle α.

where

$$\Omega : \frac{z - \frac{D}{2}}{x} < \tan(\Theta) < \frac{z + \frac{D}{2}}{x} \tag{A4}$$

and

$$0 < |\mathbf{V}| < \infty . \tag{A5}$$

This integration produces the solution for a single, straight jet with the mean inlet velocity U_0. The final expressions for density, velocity, and temperature can be found in the work of Cai and Boyd.[34]

Similar effusion problems can be solved by altering the integration domain Ω. As described below, we adapt the solution for a single straight jet to (i) a single inclined jet and then (ii) two inclined jets next to each other.

1. Single inclined jet

To evaluate the number density of an inclined jet, the coordinate system needs to be rotated to align the jet axis with the direction of the inlet velocity (Fig. 17) using the rotation matrix

$$\mathbf{R} = \begin{pmatrix} \cos(\alpha) & -\sin(\alpha) \\ \sin(\alpha) & \cos(\alpha) \end{pmatrix}, \tag{A6}$$

where α is the inclination angle of the jet. The local coordinate transformation for integration for the upper jet is $\mathbf{r}' = \mathbf{R}\mathbf{r}$ and for the lower jet $\mathbf{r}'' = \mathbf{R}^T\,\mathbf{r}$. (For brevity, we give only the solution for the upper jet when $\alpha < 0$, as shown in Fig. 18, the solution for $\alpha > 0$ can be obtained by switching Θ_1 and Θ_2.) The integration domain at the inlet boundary has to be split into two different sections as shown on the left in Fig. 18: the inlet region where $x' < r_x$ so that the mean inlet velocity U_0 is directed toward r_x (colored in green, Ω_1 in velocity space) and that where $x' > r_x$ so that the flow will not pass r_x after leaving the inlet (hatched in blue, Ω_2 in velocity space). The corresponding domains in velocity space are shown in Fig. 18 on the right, where Ω_1 is limited by the direction vector between the upper boundary A and the studied point X shifted from the origin by $-U_0$ and a right angle, while Ω_1 is limited by the direction vector between the upper boundary B and the studied point X shifted from the origin by $+U_0$ and a right angle. In the other directions, the integration domain is unbounded. This can be transformed to polar coordinates, producing the limiting angles

$$\Theta_1 = \arctan\left(\frac{z' - \cos(\alpha)D/2}{x' + \sin(\alpha)D/2}\right), \tag{A7}$$

$$\Theta_2 = \arctan\left(\frac{z' + \cos(\alpha)D/2}{x' - \sin(\alpha)D/2}\right). \tag{A8}$$

The green integration domain Ω_1 is then given by

$$\Omega_1 : \Theta_1 < \Theta < \min\left(\frac{\pi}{2}, \Theta_2\right), \tag{A9}$$

$$|\mathbf{V}_1| = \sqrt{(c_x + U_0)^2 + c_z^2}, \tag{A10}$$

and the blue hatched integration domain Ω_2 by

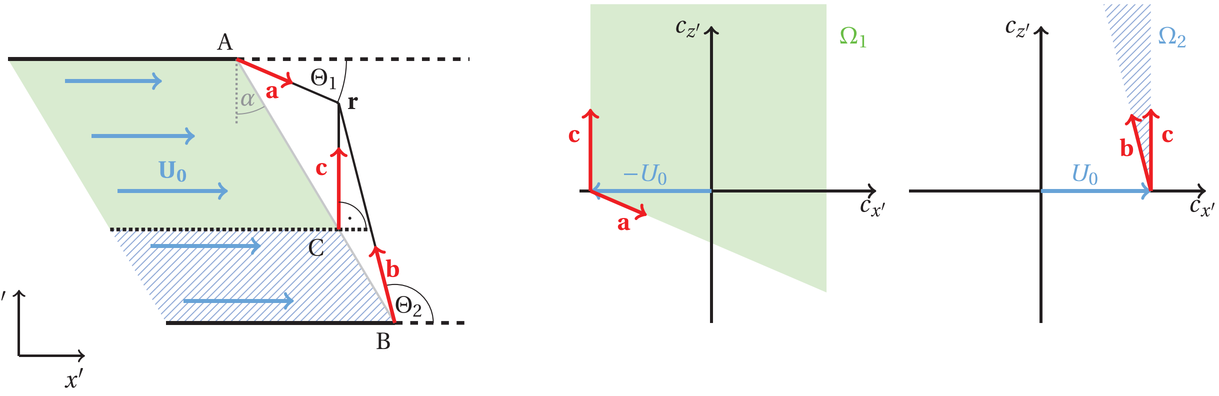

FIG. 18. Single jet. On the left is a sketch of the jet geometry in real space, and on the right, there are the two velocity domains compared to Fig. 16. To obtain the solution at point **r**, the integration domain is split into a part where the mean inlet velocity is directed toward **r** (uniform green area) and one where the mean inlet velocity is directed away from **r** (hatched in blue area).

$$\Omega_2 : \frac{\pi}{2} < \Theta < \Theta_2 \,, \tag{A11}$$

$$|\mathbf{V_2}| = \sqrt{(c_x - U_0)^2 + c_z^2}\,. \tag{A12}$$

All solutions can be written as a function of the inlet speed ratio $S_0 = U_0/\sqrt{2k_BT/m}$ and the angles Θ_1, Θ_2. To switch between regions where only the green depicted integration domain Ω_1 and the one where also Ω_2 has to be considered, the Heaviside step function $H()$ is applied. The expressions for number density $n(x, z)$, velocities $u(x, z), w(x, z)$, and total energy $E_{tot}(x, z)$ of a single inclined plume then read

$$\begin{aligned}\frac{n(x,z)}{n_0} = {} & \frac{\exp\left(-S_0^2\right)}{2\pi}(\Theta_2 - \Theta_1) \\ & + \frac{1}{4}[\mathrm{erf}(S_0 \sin\Theta_2) - \mathrm{sign}(\Theta_1)\mathrm{erf}(S_0 \sin\Theta_1)] \\ & + H\left(\Theta_2 - \frac{\pi}{2}\right)\frac{1}{2}[\mathrm{erf}(S_0) - \mathrm{erf}(S_0 \sin\Theta_2)] \\ & + \frac{S_0}{2\pi}\int_{\Theta_1}^{\Theta_2} \exp\left(-S_0^2 \sin^2\Theta\right)\cos\Theta\,\mathrm{erf}(S_0\cos\Theta)\,\mathrm{d}\Theta\,,\end{aligned} \tag{A13}$$

$$\begin{aligned}\frac{u(x,z)}{\sqrt{2k_BT_0/m}} = {} & \frac{\exp\left(-S_0^2\right)}{\pi n(x,z)}\left[\frac{S_0}{2}\left(\Theta_2 - \Theta_1 + H\left(\Theta_2 - \frac{\pi}{2}\right)(\pi - 2\Theta_2)\right) + \frac{S_0}{4}\left(\sin(2\Theta_2) - \sin(2\Theta_1) - H\left(\Theta_2 - \frac{\pi}{2}\right)2\sin(2\Theta_2)\right)\right. \\ & + S_0^2\sqrt{\pi}\left(\int_{\Theta_1}^{\Theta_2} \cos^3\Theta(1 + \mathrm{erf}(S_0\cos\Theta))\exp\left(S_0^2\cos^2\Theta\right)\mathrm{d}\Theta - H\left(\Theta_2 - \frac{\pi}{2}\right)2\int_{\frac{\pi}{2}}^{\Theta_2} \cos^3\Theta\,\mathrm{erf}(S_0\cos\Theta)\exp\left(S_0^2\cos^2\Theta\right)\mathrm{d}\Theta\right) \\ & \left. + \frac{\sqrt{\pi}}{2}\left(\int_{\Theta_1}^{\Theta_2} \exp\left(S_0^2\cos^2\Theta\right)\cos\Theta(1 + \mathrm{erf}(S_0\cos\Theta))\,\mathrm{d}\Theta - H\left(\Theta_2 - \frac{\pi}{2}\right)2\int_{\frac{\pi}{2}}^{\Theta_2} \exp\left(S_0^2\cos^2\Theta\right)\cos\Theta\,\mathrm{erf}(S_0\cos\Theta)\,\mathrm{d}\Theta\right)\right],\end{aligned} \tag{A14}$$

$$\begin{aligned}\frac{w(x,z)}{\sqrt{2k_BT_0/m}} = {} & \frac{1}{4\sqrt{\pi}n(x,z)} \cdot \left[\exp\left(-S_0^2\sin^2\Theta_1\right)\cos\Theta_1(1 + \mathrm{erf}(S_0\cos\Theta_1)) - \exp\left(-S_0^2\sin^2\Theta_2\right)\cos\Theta_2(1 + \mathrm{erf}(S_0\cos\Theta_2))\right. \\ & \left. + H\left(\Theta_2 - \frac{\pi}{2}\right)2\exp\left(-S_0^2\sin^2\Theta_2\right)\cos\Theta_2\,\mathrm{erf}(S_0\cos\Theta_2)\right],\end{aligned} \tag{A15}$$

$$\begin{aligned}E_{tot}(x,z) = {} & \frac{T_0\exp\left(-S_0^2\right)}{6n(x,z)\pi}\left[\left(3 + S_0^2\right)(\Theta_2 - \Theta_1) + S_0^2\left(\frac{1}{2}(\sin 2\Theta_2 - \sin 2\Theta_1)\right)\right. \\ & + 2S_0\sqrt{\pi}\int_{\Theta_1}^{\Theta_2}\left(2\cos\Theta + S_0^2\cos^3\Theta\right)\exp\left(S_0^2\cos^2\Theta\right)(1 + \mathrm{erf}(S_0\cos\Theta))\,\mathrm{d}\Theta \\ & \left. - H\left(\Theta_2 - \frac{\pi}{2}\right)4S_0\sqrt{\pi}\int_{\Theta_2}^{\frac{\pi}{2}}\left(2\cos\Theta + S_0^2\cos^3\Theta\right)\exp\left(S_0^2\cos^2\Theta\right)\mathrm{d}\Theta\right].\end{aligned} \tag{A16}$$

2. Superposition of two inclined jets

The number density of the interacting case is the superposition of number densities of two single jets given by

$$n(\mathbf{r}) = n_U(\mathbf{r}) + n_L(\mathbf{r})\,, \tag{A17}$$

where the subscript U denotes the upper jet and L the lower one. The velocity vectors have to be rotated back into the original coordinate system by

$$\mathbf{u_U} = \mathbf{R}^T\,\mathbf{u}'_\mathbf{U} \quad \text{and} \quad \mathbf{u_L} = \mathbf{R}\,\mathbf{u}''_\mathbf{L}\,, \tag{A18}$$

before applying their density-weighted average to obtain the velocity of the jet interaction

$$\mathbf{u}(\mathbf{r}) = \frac{n_U(\mathbf{r})\mathbf{u_U}(\mathbf{r}) + n_L(\mathbf{r})\mathbf{u_L}(\mathbf{r})}{n(\mathbf{r})}\,. \tag{A19}$$

To obtain the temperature field, the thermal energy is calculated as the difference of the total energy of both jets E_{tot} and the macroscopic kinetic energy E_{kin} derived from the velocity and number density field,

$$E_{tot}(\mathbf{r}) = m\iiint_{\Omega_U\cup\Omega_L}\xi^2 f_0(\xi)\,\mathrm{d}\xi\,, \tag{A20}$$

$$E_{kin}(\mathbf{r}) = m\,n(\mathbf{r})\,\mathbf{u}(\mathbf{r})^2\,. \tag{A21}$$

The temperature field is then determined by

TABLE III. Overview of tested solvers.

	Cells	Temporal integration	CFL	Convective scheme	Advective schemes	Grad scheme
sonicFoam (foam-extend 4.0)	50 000	Euler	0.1	cell Limited linear 1	van Leer	cell Limited linear 1
dbnsFoam (foam-extend 4.0)	150	Runge–Kutta 4	Flux based	Flux: rusanov, Limiter: Barth–Jespersen	...	...
dbnsFoam hllc	150, 10 000, 100 000	Runge–Kutta 4	Flux based	Flux: HLLC, Limiter: Barth–Jespersen	...	...
rhoCentralFoam (OpenFoam v18.06)	1000	Euler	0.1	Flux: Tadmor	...	cellLimited least Squares 1

$$T = \frac{1}{3k_B n(\mathbf{r})}\left(E_{tot}(\mathbf{r}) - E_{kin}(\mathbf{r})\right). \tag{A22}$$

The same steps can be conducted to adapt the effusion solution for three-dimensional single plumes[64] to interacting three-dimensional plumes.

APPENDIX B: VERIFICATION RIEMANN SOLVER, SHOCK TUBE

We verified the approximate Riemann solver using a shock tube case, which is 1D domain initially split in a high- and a low-pressure section by a membrane. The sudden destruction of the membrane yields an expansion wave traveling into the high-pressure section (driver section) and a shock wave traveling into the low-pressure region (driven section) until they reach their respective boundaries. The shock tube setup is often used to test compressible solvers and schemes, as it is simple, but still covers all fundamental phenomena in compressible flow, i.e., expansion wave, contact discontinuity, and shock.

We tested multiple compressible solvers and schemes available in OpenFoam, as listed in Table III. The classical Sod's shock tube test is driven by a pressure ratio of 10, for which most of the compressible solvers mentioned hereafter produced reasonable to accurate results.[65,66] However, the tremendous pressure ratio due to the vacuum exacerbates the problem so that the shock is not captured accurately anymore. To verify the solver for the case of interacting jets, we adapted the shock tube test case to a pressure ratio of 5×10^5, which is an extreme version of the simulated cases. The computational domain and initial conditions are depicted in Fig. 19. No initial or inlet velocity is assumed. The high pressure

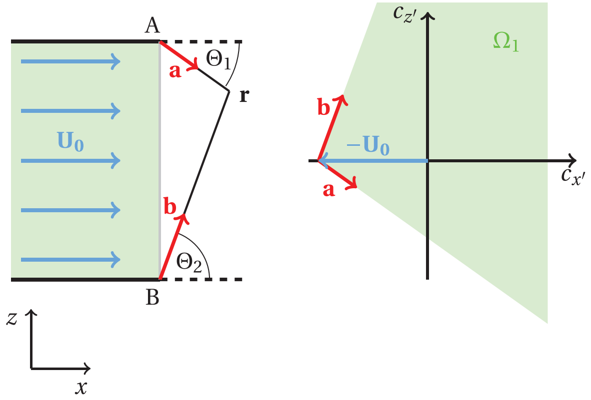

FIG. 19. Sketch of the shock tube. Driver section on the left; driven section on the right.

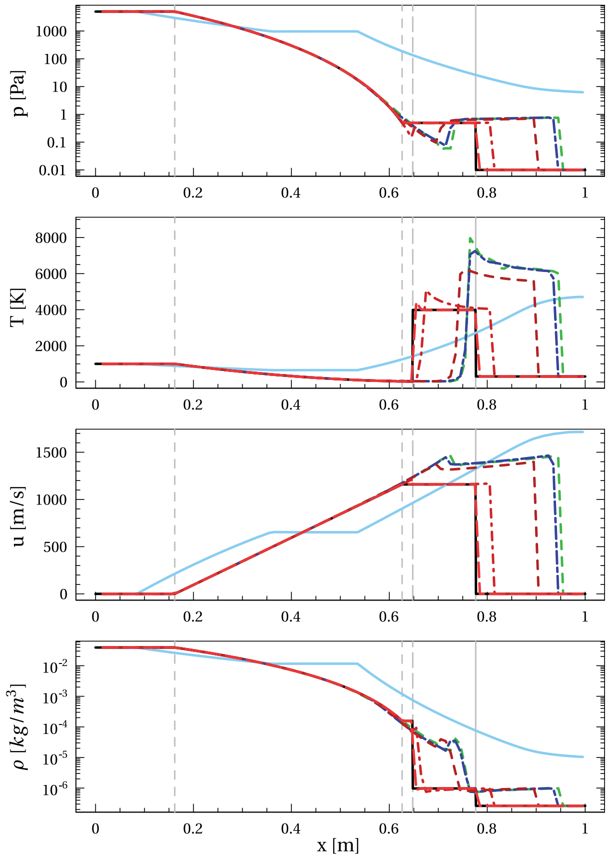

FIG. 20. Pressure, temperature, velocity, and density profiles in the shock tube at $t = 0.0003$ s from the analytical solution and different solvers. The thin gray lines mark from left to right: the expansion head, the expansion tail, the slip surface, and the shock.

ratio in the driven section may give rise to numerical instabilities, i.e., either oscillations or over-/undershoots. In addition, it should be noted that the smaller the sound speed ratio between the driver and driven section a_1/a_4 (below unity), the stronger the shock and the higher the minimum temperature in the expansion wave, which may yield negative temperatures for an insufficient discretization.

Figure 20 shows the pressure, temperature, velocity, and density profiles for the analytical solution[58] and different solvers at $t = 0.0003$ s. The result of sonicFoam, which is a pressure-based solver, is far from the solution and does not capture the shock features even in qualitative terms (please note that this is the version in foam-extend 4.0, which differs from the in ESI OpenFoam versions). rhoCentralFoam, a solver based on Tadmor flux splitting, qualitatively captures the expansion and shock, but overpredicts shock speed. Further grid refinement produces oscillations around the discontinuities, which results in the divergence of the solver. dbnsFoam, an approximate Riemann solver, produces a result similar to rhoCentralFoam, when a Rusanov flux scheme is applied. When a HLLC flux is applied, the shock speed is reduced. Grid refinement further improves the prediction. However, to obtain a reasonably accurate solution, 100*k* cells are required, which is immense for a 1D problem and illustrates the difficulties in using CFD for high pressure ratios.

APPENDIX C: MESH INDEPENDENCE STUDY

The independence of the solution from the mesh was studied. The computational domain was chosen a bit longer than for the DSMC solution and was 0.012 × 0.03 m. All tested meshes had a completely orthogonal and equidistant meshing to ensure perfect orthogonality and a fine resolution along the entire shock at the same time. The resolution for the studied meshes is listed in Table IV. Figure 21 shows the normalized density and deposition rate predicted on the three different meshes at $x = 15$ mm. To highlight the small differences, only the region above the symmetry line is considered. The coarse mesh predicts the height of the two plateaus before and after the shock correctly, but calculates a lower steepness across the shock and a larger density drop around the symmetry compared with the medium and fine mesh. The solution on the medium and fine mesh matches quite well. For the normalized deposition rate, the parameter which was of foremost importance in this study, the small deviations in density rate are mitigated producing a good match between all meshes and an excellent match between the medium and fine mesh. Hence, the medium mesh was chosen for all calculations.

TABLE IV. Mesh parameters for mesh independence study for the approximate Riemann solver.

	Cells	Cells in x-direction	Cells in z-direction
Coarse	288 000	1200	240
Medium	1 152 000	2400	480
Fine	1 792 000	3200	560

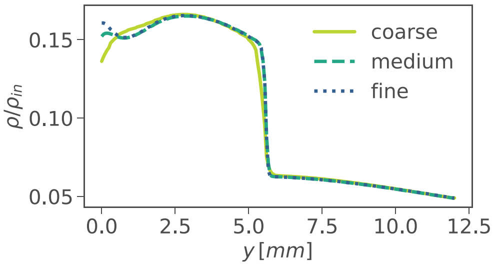

(a)

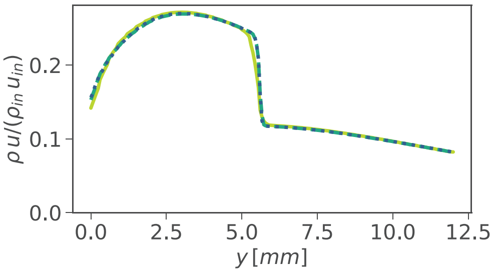

(b)

FIG. 21. Profiles of (a) normalized density and (b) normalized deposition rate for different mesh refinements at $x = 15$ mm for the inviscid continuum flow (Riemann solver, inlet density corresponds to the case $Kn_s = 8Kn_0$). (a) Density at $x = 15$ mm and (b) deposition rate at $x = 15$ mm.

APPENDIX D: SHOCK STRUCTURE

To validate the shock detection method and to gain a better understanding of the shock region, we analyze the changes the flow undergoes when passing through the shock. Figure 22 compares the inviscid continuum solution and one rarefied solution for $Kn_s = 2Kn_0$. Figures 22(a) and 22(b) show the subsonic region (red dots), the detected shock (blue solid line), and multiple streamlines crossing the shock. The changes the flow undergoes within the shock are shown for streamline No. 0 in Fig. 22(c) for the inviscid continuum solution and in Fig. 22(d) for the transitional flow regime. The figures show the profiles of several flow variables $\Phi \in [n, T, M, \ldots]$ in the immediate vicinity of the shock, normalized by their local maximum and minimum values before (Φ_1) and after the shock (Φ_2), which reads

$$\tilde{\Phi} = \frac{\Phi - \Phi_1}{\Phi_2 - \Phi_1}.$$

First, we focus on the number density profile, as it is commonly used to define the shock position and shock thickness.[39] Before the shock, the number density declines due to expansion—which is more clearly visible in the transitional flow regime as the shown section covers a longer streamline length—and rises sharply in the shock. Its crossing of $\tilde{n} = 0.5$ is commonly picked as shock location and here marked by gray dashed lines. The blue vertical line marks the location where the shock was detected by our proposed approach using the MOC. The detected location varied between $\tilde{n} \approx 0.3 - 0.8$ for the streamlines shown, with the exception of

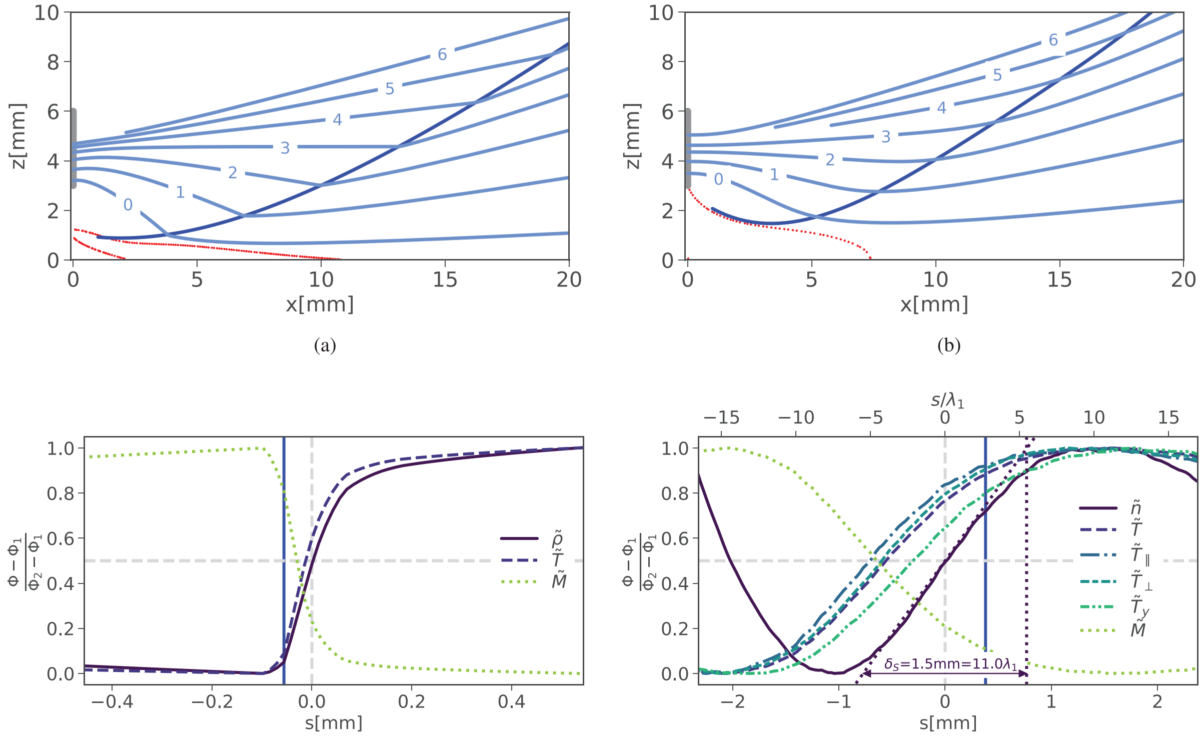

FIG. 22. (a) and (b) Streamline positions. (c) and (d) Profiles along the streamlines across the shock. The vertical blue line marks the detected shock location; the gray dashed lines mark the actual shock location, i.e., $\tilde{n} = 0.5$. (a) Streamlines for $Kn_s = 2Kn_0$. Inviscid continuum solution. The gray solid line marks the inlet position, the light blue solid lines mark streamlines, and the blue solid line denotes the detected shock position and the red dots represent the sonic line. (b) Streamlines for $Kn_s = 2Kn_0$. DSMC solution. The gray solid line marks the inlet position, the light blue solid lines mark streamlines, and the blue solid line denotes the detected shock position and the red dots represent the sonic line. (c) Flow variables plotted over streamline No. 0 in subfigure (a) around the shock position for $Kn_s = 2Kn_0$ (Euler solution). (d) Flow variables plotted over streamline No. 0 in subfigure (b) around the shock position for $Kn_s = 2Kn_0$ (DSMC solution).

streamline No. 0 for the continuum flow with $\tilde{n} \approx 0$, for which the broad region of converging characteristics around the subsonic region hampers localization.

The shock thickness δ_s is the distance it takes to go from pre-shock density to post-shock density when applying the highest slope of the density profile inside the shock, i.e.,

$$\delta_s = \left[\max\left(\frac{\mathrm{d}\tilde{n}}{\mathrm{d}s}\right)\right]^{-1}.$$

Since the change from pre-shock to post-shock state depends on the number of collisions undergone, the shock thickness is commonly expressed in terms of mean free path lengths from the pre-shock state, λ_1. (For inviscid continuum flow, the shock thickness vanishes, and the continuity of the shown profiles is due to discretization.) Streamline No. 0 is near the subsonic region for both the continuum and the transitional flow regime. It enters the shock at a wide angle and bends more than the other depicted streamlines. For the case in the transitional flow regime, the shock thickness is $\delta_S = 1.5\,\mathrm{mm}$, which corresponds to $11\lambda_1$. Considering that the shock is a weak oblique shock with a pre-shock Mach $M_1 = 2.4$ and post-shock Mach $M_2 = 1.3$, the thickness compares reasonably well with typical thicknesses for weak normal shocks.[67,70]

The Mach number drops and the temperature rises before the number density rise occurs. The shift between the temperature and density profile is about $5\lambda_1$ for the transitional flow regime. While in a continuum, only one equilibrium temperature is defined, the different temperature modes are shifted as well for transitional flow. We split the temperature in a temperature which is parallel to the local mean velocity, denoted as $T_\parallel$, one orthogonal to it (but in the solution plane), denoted as $T_\perp$, and one in the quasi-homogeneous out-of-plane direction, denoted as T_y. First, the parallel temperature $T_\parallel$ rises, as the decrease in mean velocity due to the mixing of pre-shock and post-shock particles is reflected in a transfer from macroscopic kinetic energy to thermal energy. The orthogonal temperature follows closely, one reason being that the streamline bending breaks the alignment of particle velocities with the mean velocity. (If collisions played the dominant role in this initial rise of parallel and orthogonal temperatures, the equidistribution between modes would transfer the energy to the homogeneous direction immediately.) Only then does the temperature in homogeneous direction rise due to collisions, which transfer the energy from the parallel and orthogonal temperature mode into the homogeneous direction. This temperature–density separation of $2-3\lambda_1$ between temperatures is maintained across the shock, which indicates that the free movement of particles between two collisions introduces non-equilibrium, which cannot be overcome by the redistribution due to collisions (no comprehensive experimental measurements are available). The temperature–density separation in oblique shocks is expected to increase with the velocity component tangential to the shock.)

DATA AVAILABILITY

The data that support the findings of this study are available from the corresponding author upon reasonable request.

REFERENCES

[1] B. Doncaster, J. Shulman, J. Bradford, and J. Olds, "Spaceworks' 2016 nano/microsatellite market forecast" (SpaceWorks Enterprises, Inc., Atlanta, GA, 2016).

[2] A. Z. Giovannini and R. S. Abhari, "Rarefied flow expansion in linear aerospikes," Phys. Fluids **27**, 062003 (2015).

[3] E. Zoestbergen, T. Maalman, C. Commandeur, and M. Goodenough, "Influence of contamination on the thermal evaporation of a zinc melt," Surf. Coat. Technol. **218**, 108–113 (2013).

[4] J. E. Vesper, C. S. Obiji, R. Westerwaal, C. Boelsma, S. Kenjereš, and C. R. Kleijn, "Modeling of a continuous physical vapor deposition process: Mass transfer limitations by evaporation rate and sonic choking," Appl. Therm. Eng. **195**, 117099 (2021).

[5] Z. Yang, Z.-Y. Tang, G.-B. Cai, and B.-J. He, "Development of a coupled NS-DSMC method for the simulation of plume impingement effects of space thrusters," Thermophys. Aeromech. **24**, 835–847 (2017).

[6] K. H. Lee, "Plume simulation of liquid apogee engine for GEO satellite using parallel DSMC method," Comput. Fluids **208**, 104612 (2020).

[7] A. Zilic, D. Hitt, and A. Alexeenko, "Numerical simulations of supersonic flow in a linear aerospike micro nozzle," AIAA Paper No. 2007-3984, 2007.

[8] K. H. Lee, "Numerical comparison of exhaust plume flow behaviors of small monopropellant and bipropellant thrusters," PLoS One **12**, e0176423 (2017).

[9] A. K. Chinnappan, R. Kumar, and V. K. Arghode, "Modeling of dusty gas flows due to plume impingement on a lunar surface," Phys. Fluids **33**, 053307 (2021).

[10] V. Yarygin, Y. I. Gerasimov, A. Krylov, V. Prikhodko, A. Y. Skorovarov, and I. Yarygin, "Model and on-orbit study of the international space station contamination processes by jets of its orientation thrusters," J. Phys.: Conf. Ser. **925**, 012003 (2017).

[11] V. Yarygin, V. Prikhodko, and I. Yarygin, "Modeling of space vehicle orientation thruster jets in vacuum chambers," J. Appl. Mech. Tech. Phys. **61**, 798–806 (2020).

[12] R. Jambunathan and D. A. Levin, "On the study of ion thruster plume characteristics and backflow contamination using fully kinetic PIC-DSMC simulations," AIAA Paper No. 2019-3991, 2019.

[13] M. Grabe and C. E. Soares, "Status and future of research on plume induced contamination," in *Proceedings of the International Astronautical Congress, IAC* (IAF, 2019), pp. 1–15.

[14] C. Cai and X. He, "Detailed flowfield and surface properties for high Knudsen number planar jet impingement at an inclined flat plate," Phys. Fluids **28**, 056103 (2016).

[15] S. Cai, C. Cai, and J. Li, "Jet loads on a plate with different Knudsen numbers," Phys. Fluids **30**, 127101 (2018).

[16] P. J. Herráiz, J. M. Fernández, and J. R. Villa, "Development of a MATLAB® plume impingement tool for fast system analysis," in Proceedings of the 8th European Conference for Aeronautics and Aerospace Sciences (EUCASS) (2019).

[17] B. Zitouni, F. Weber, and R. Kast, "CFD and DSMC methods for tracking gases and droplets behaviors within the plume," Proc. SPIE **11489**, 114890C (2020).

[18] J. Berg, D. Goldstein, P. Varghese, and L. Trafton, "DSMC simulation of Europa water vapor plumes," Icarus **277**, 370–380 (2016).

[19] W. J. McDoniel, D. B. Goldstein, P. L. Varghese, and L. M. Trafton, "Simulation of Io's plumes and Jupiter's plasma torus," Phys. Fluids **31**, 077103 (2019).

[20] W. A. Hoey, L. M. Trafton, P. C. Ackley, D. B. Goldstein, and P. L. Varghese, "Variations in the canopy shock structures of massive extraterrestrial plumes: Parametric DSMC simulation of 2007 Tvashtar observations," Icarus **363**, 114431 (2021).

[21] T. Soga, M. Takanishi, and M. Yasuhara, "Experimental study of underexpanded free jets," in Proceedings of 14th International Symposium on Rarefied Gas Dynamics, Tsukuba Science City, Japan, 1984.

[22] I. A. Chirokov, T. G. Elizarova, J.-C. Lengrand, I. Gibek, and I. A. Graur, "Experimental and numerical investigation of rarefied interacting plumes," AIP Conf. Proc. **663**, 572–579 (2003).

[23] G. Koppenwallner, "Scaling laws for rarefied plume interference with application to satellite thrusters," in Proceedings of 14th International Symposium on Space Technology and Science, Tokyo, Japan (1984), pp. 505–512.

[24] L. Dagum and S. K. Zhu, "Direct simulation Monte Carlo simulation of the interaction between rarefied free jets," J. Spacecr. Rockets **31**, 960–964 (1994).

[25] A. Holz, G. Dettleff, K. Hannemann, and S. Ziegenhagen, "Experimental investigation of two interacting thruster-plumes downstream of the nozzles," in Proceedings of Space Propulsion (2012).

[26] W. Li and F. Ladeinde, "Simulation and analysis of rarefied parallel interacting sonic jets," AIAA Paper No. 2006-1192, 2006.

[27] S. Zhu and L. Dagum, "Self-similarity in rarefied jet interactions: A DSMC study," in *Proceedings of 30th Thermophysics Conference* (AIAA, 1995), p. 2030.

[28] A. Venkattraman and A. A. Alexeenko, "Direct Simulation Monte Carlo modeling of metal vapor flows in application to thin film deposition," Vacuum **86**, 1748 (2012).

[29] A. V. Y. Baby and B. Rajesh, "Experimental study on the interaction of underexpanded jets in rarefied flow regimes," in *Proceedings of 30th International Symposium on Shock Waves 2* (Springer, 2017), pp. 859–867.

[30] J. Allègre, A. Chaiz, I. Chirokov, N. Gorchakova, I. Graur, C. Purpura, I. Gibek, T. Elizarova, and J.-C. Lengrand, "Numerical and experimental investigation of plumes interacting with satellite walls," Spacecr. Propul. **465**, 619 (2000), see http://adsabs.harvard.edu/pdf/2000ESASP.465..619A.

[31] W. Li and F. Ladeinde, "Analysis of interacting, underexpanded, rarefied jets," AIAA J. **49**, 2581–2585 (2011).

[32] M. Grabe, G. Dettleff, and K. Hannemann, "Impact of nozzle separation on the plumes of two parallel thrusters," AIP Conf. Proc. **1786**, 170005 (2016).

[33] M. Knudsen, "Die Gesetze der Molekularströmung und der inneren Reibungsströmung der Gase durch Röhren," Ann. Phys. **333**, 75–130 (1909).

[34] C. Cai and I. D. Boyd, "Theoretical and numerical study of free-molecular flow problems," J. Spacecr. Rockets **44**, 619–624 (2007).

[35] R. Vos and S. Farokhi, *Introduction to Transonic Aerodynamics* (Springer, 2015), Vol. 110.

[36] v. L. Crocco, "Eine neue Stromfunktion für die Erforschung der Bewegung der Gase mit Rotation," ZAMM **17**, 1–7 (1937).

[37] M. J. Zucrow and J. D. Hoffman, *Gas Dynamics Volume 2—Multidimensional Flow* (Wiley, 1977).

[38] M. Silnikov, M. Chernyshov, and V. Uskov, "Analytical solutions for Prandtl–Meyer wave–oblique shock overtaking interaction," Acta Astronaut. **99**, 175–183 (2014).

[39] H. Alsmeyer, "Density profiles in argon and nitrogen shock waves measured by the absorption of an electron beam," J. Fluid Mech. **74**, 497–513 (1976).

[40] M. Kanamori and K. Suzuki, "Shock wave detection in two-dimensional flow based on the theory of characteristics from CFD data," J. Comput. Phys. **230**, 3085–3092 (2011).

[41] M. Kanamori and K. Suzuki, "Shock wave detection based on the theory of characteristics," in *Shock Fitting: Classical Techniques, Recent Developments, and Memoirs of Gino Moretti*, edited by M. Onofri and R. Paciorri (Springer International Publishing, Cham, 2017), pp. 171–190.

[42] foam-extend-4.0, https://sourceforge.net/p/foam-extend/foam-extend-4.0/ci/master/tree/ReleaseNotes.txt (2016).

[43] E. F. Toro, M. Spruce, and W. Speares, "Restoration of the contact surface in the HLL-Riemann solver," Shock Waves **4**, 25–34 (1994).

[44] S. Dellacherie, "Analysis of Godunov type schemes applied to the compressible Euler system at low Mach number," J. Comput. Phys. **229**, 978–1016 (2010).

[45] E. F. Toro, "Riemann problems and the WAF method for solving the two-dimensional shallow water equations," Philos. Trans. R. Soc., A **338**, 43–68 (1992).
[46] K. Xu and J.-C. Huang, "A unified gas-kinetic scheme for continuum and rarefied flows," J. Comput. Phys. **229**, 7747–7764 (2010).
[47] X. K, *Direct Modeling for Computational Fluid Dynamics: Construction and Application of Unified Gas-Kinetic Schemes* (World Scientific, 2014), Vol. 4.
[48] Z. Guo, R. Wang, and K. Xu, "Discrete unified gas kinetic scheme for all Knudsen number flows. II. Thermal compressible case," Phys. Rev. E **91**, 033313 (2015).
[49] Y. Zhang, L. Zhu, R. Wang, and Z. Guo, "Discrete unified gas kinetic scheme for all Knudsen number flows. III. Binary gas mixtures of Maxwell molecules," Phys. Rev. E **97**, 053306 (2018).
[50] X. Zhao, C. Wu, Z. Chen, L. Yang, and C. Shu, "Reduced order modeling-based discrete unified gas kinetic scheme for rarefied gas flows," Phys. Fluids **32**, 067108 (2020).
[51] S. Chen, K. Xu, and Q. Cai, "A comparison and unification of ellipsoidal statistical and Shakhov BGK models," Adv. Appl. Math. Mech. **7**, 245–266 (2015).
[52] B. N. Todorova, C. White, and R. Steijl, "Numerical evaluation of novel kinetic models for binary gas mixture flows," Phys. Fluids **32**, 016102 (2020).
[53] L. Zhu, X. Pi, W. Su, Z.-H. Li, Y. Zhang, and L. Wu, "General synthetic iterative scheme for nonlinear gas kinetic simulation of multi-scale rarefied gas flows," J. Comput. Phys. **430**, 110091 (2021).
[54] S. Plimpton, S. Moore, A. Borner, A. Stagg, T. Koehler, J. Torczynski, and M. Gallis, "Direct simulation Monte Carlo on petaflop supercomputers and beyond," Phys. Fluids **31**, 086101 (2019).
[55] G. Bird, *Molecular Gas Dynamics and the Direct Simulation of Gas Flows* (Clarendon Press, , Oxford, 1994).
[56] C. White, M. K. Borg, T. J. Scanlon, S. M. Longshaw, B. John, D. Emerson, and J. M. Reese, "dsmcFoam+: An OpenFOAM based direct simulation Monte Carlo solver," Comput. Phys. Commun. **224**, 22–43 (2018).
[57] F. P. Boynton, "Highly underexpanded jet structure: Exact and approximate calculations," AIAA J. **5**, 1703–1704 (1967).
[58] J. D. Anderson, *Modern Compressible Flow* (Tata McGraw-Hill Education, 2003).
[59] T. J. Poinsot and S. Lelef, "Boundary conditions for direct simulations of compressible viscous flows," J. Comput. Phys. **101**, 104–129 (1992).
[60] J. Fan, I. D. Boyd, and C. Shelton, "Monte Carlo modeling of electron beam physical vapor deposition of yttrium," J. Vac. Sci. Technol., A **18**, 2937–2945 (2000).
[61] P. Fialho, J. Fareleira, M. Ramires, and C. A. Nieto de Castro, "Thermophysical properties of alkali metal vapours Part I.A: Prediction and correlation of transport properties for monatomic systems," Ber. Bunsengesellschaft Phys. Chem. **97**, 1487–1492 (1993).
[62] H. Struchtrup, "Macroscopic transport equations for rarefied gas flows," in *Macroscopic Transport Equations for Rarefied Gas Flows* (Springer, 2005), pp. 145–160.
[63] W. Stein and A. Alexeenko, "Application of the DSMC method for design of a coaxial microthruster nozzle," AIAA Paper No. 2008-4530, 2008.
[64] C. Cai and L. Wang, "Numerical validations for a set of collisionless rocket plume solutions," J. Spacecr. Rockets **49**, 59–68 (2012).
[65] A. R. Khodadadi, M. R. Malekbala, and A. F. Khodadadi, "Evaluate shock capturing capability with the numerical methods in OpenFOAM," Therm. Sci. **17**, 1255–1260 (2013).
[66] M. H. Arabnejad, R. Bensow, and C. Eskilsson, "Density-based compressible solver with equilibrium cavitation model in OpenFoam," in Proceedings of 19th Numerical Towing Tank Symposium-NuTTS, St Pierre D'Oleron, France, 2016.
[67] C. Cercignani, *Rarefied Gas Dynamics: From Basic Concepts to Actual Calculations* (Cambridge University Press, 2000), Vol. 21.
[68] A. Holz, "Experimentelle Untersuchungen zur Abgasstrahl-Wechselwirkung von zwei Kleintriebwerken unter weltraumähnlichen Hochvakuumbedingungen," Ph.D. thesis (University of Stuttgart, 2012).
[69] S. Ivanov, N. Markelov, V. Kashkovsky, and D. Giordano, "Numerical analysis of thruster plume interaction problems," in *Proceedings of European Spacecraft Propulsion Conference* [European Space Agency (ESA), 1997], Vol. 398, p. 603.
[70] R. Sambasivam, "Extended Navier–Stokes equations: Derivations and applications to fluid flow problems," Ph.D. thesis (University of Erlangen, 2013).
[71] E. F. Toro, *Riemann Solvers and Numerical Methods for Fluid Dynamics: A Practical Introduction* (Springer Science & Business Media, 2013).
[72] V. Pasquariello, S. Hickel, and N. A. Adams, "Unsteady effects of strong shock-wave/boundary-layer interaction at high Reynolds number," J. Fluid Mech. **823**, 617–657 (2017).